

<sub>1</sub> Physics-Infused Reduced-Order Modeling for Analysis of  
<sub>2</sub> Ablating Hypersonic Thermal Protection Systems

<sub>3</sub>

<sub>4</sub> November 24, 2025

<sub>5</sub>

## Abstract

This work presents a *physics-infused reduced-order modeling* (PIROM) framework towards design, analysis, and optimization of non-decomposing ablating hypersonic thermal protection systems (TPS), and is demonstrated via the modeling of transient thermo-ablative responses of multi-layered hypersonic TPS. The PIROM architecture integrates a reduced-physics backbone, based on the lumped-capacitance model (LCM) and a surface recession model (SRM), with data-driven correction dynamics formulated via a coarse-graining approach rooted in the Mori-Zwanzig formalism. The LCM is coupled to the SRM to capture the one-dimensional surface recession of the ablating TPS as a function of the surface temperature. While the LCM and SRM capture the dominant physics of the ablating TPS response, the correction terms compensate for residual dynamics arising from higher-order non-linear interactions and temperature-advection effects due to surface recession. The PIROM consistently achieves errors of  $\approx 0.5\%$  for a wide range of extrapolative settings of design parameters involving time-and-space varying boundary conditions and SRM models, and improves by an order of magnitude by the LCM alone. Moreover, the PIROM delivers online evaluations that are two orders of magnitude faster than the full-order model (FOM). These results demonstrate that PIROM effectively reconciles the trade-offs between accuracy, generalizability, and efficiency, providing a promising framework for optimizing multi-physical dynamical systems, such as TPS, under diverse operating conditions.

<sub>25</sub>

## 1 Introduction

<sub>26</sub> At hypersonic speeds, aerospace vehicles experience extreme aero-thermo-dynamic environments that require specialized thermal protection systems (TPS) to shield internal sub-  
<sub>27</sub> structures, electronics, and possibly crew members from the intense aerodynamic heating.  
<sub>28</sub> The TPS is often composed of ablating materials – a high-temperature capable fibrous material injected with a resin that fills the pore network and strengthens the composite [1]. The  
<sub>29</sub> TPS design promotes the exchange of mass through thermal and chemical reactions (i.e.,  
<sub>30</sub> ablation), effectively mitigating heat transfer to the sub-structures. As a result, accurate  
<sub>31</sub> prediction for the ablating TPS response under extreme hypersonic heating becomes criti-  
<sub>32</sub> cal to ensuring survivability, performance, and safety of hypersonic vehicles. Not only is it  
<sub>33</sub> necessary to assess the performance of the thermal management systems, but also the shape  
<sub>34</sub>  
<sub>35</sub>

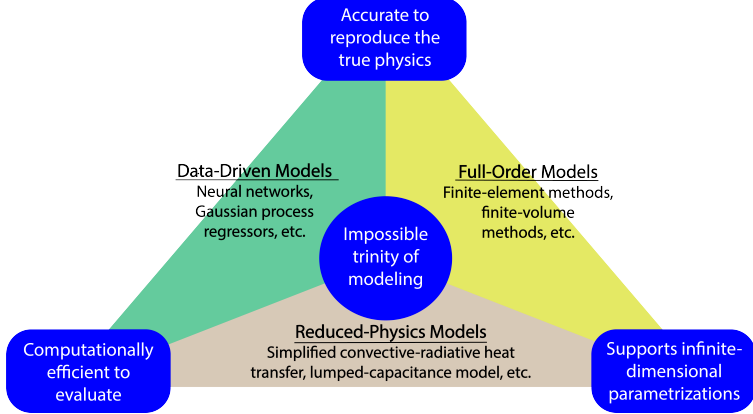


Figure 1: The impossible trinity of modeling: accuracy, generalizability, and efficiency.

36 changes of the vehicle’s outer surface induced by the ablating material, and its impact on  
37 the aerodynamics, structural integrity, and controllability.

38 Even with today’s advancements in computational resources and numerical methods,  
39 high-fidelity simulations of ablating TPS remains a formidable challenge, both theoretically  
40 and computationally. On the theoretical side, the thermo-chemical reactions, coupled with  
41 the irregular pore network structure and ablating boundaries, translate into complex non-  
42 linear equations governing multi-physical interactions across several spatio-temporal scales [1,  
43 8]. On the computational side, numerical approaches based on finite-element methods (FEM)  
44 yield semi-discrete systems of differential equations modeling the transient thermo-ablative  
45 response of the TPS [5]. The FEM discretizations lead to high-dimensional systems of  
46 equations, resulting in prohibitive computational costs for many-query applications such as  
47 design, optimization, uncertainty quantification, and real-time applications, where possibly  
48 thousands of model evaluations are required.

49 Reduced-order models (ROMs) have emerged as a promising approach to alleviate the  
50 computational costs of high-fidelity simulations [6, 11]. Ideally, a ROM should be: (1) ac-  
51 curate to reproduce high-fidelity solutions, (2) support continuous or infinite-dimensional  
52 design parameters such as geometrical shapes and material distributions, (3) be compu-  
53 tational efficient to evaluate to allow for fast turnaround times in design optimization. However,  
54 the above three capabilities usually form an *impossible trinity of modeling*, as illustrated in  
55 Fig. 1; building a ROM that achieves any two capabilities sacrifices the third.

56 The impossible trinity poses a significant challenge in the development of ROMs for the  
57 multi-disciplinary transient analysis and optimization of ablating TPS. Specifically, full-order  
58 models (FOMs), such as FEMs, offer high accuracy and robust generalization over design  
59 spaces, but are computationally expensive to evaluate. Reduced-physics models (RPMs) –  
60 such as simplified convective-radiative heat transfer or engineering correlations – are low-  
61 dimensional models that achieve efficiency and broad applicability by ignoring higher-order  
62 non-linear effects. However, RPMs sacrifice accuracy for complex thermo-ablative responses  
63 due to the simplifications and assumptions inherent in their formulation, and it is generally  
64 not clear how to systematically leverage existing high-fidelity data to improve RPMs [18].

65 Lastly, data-driven ROMs, such as Gaussian Process Regression (GPR) [? ] and neu-  
66 ral ordinary differential equations (NODEs) [3], can provide accurate and computationally-

67 efficient approximations of high-fidelity models for complex thermo-ablative responses. How-  
68 ever, these data-centric approaches often demand extensive high-fidelity data for training,  
69 do not necessarily satisfy fundamental physical constraints or conservation laws, and thus  
70 do not generalize well to the design spaces outside the training [16].

71 This work presents the extension of the *physics-infused reduced-order modeling* (PIROM)  
72 framework to include effects of ablation in for TPS applications, previously ignored in  
73 Ref. [17]. Specifically, the PIROM is demonstrated for the transient thermo-ablative re-  
74 sponse of multi-layered hypersonic TPS. The PIROM is a non-intrusive framework that  
75 combines the strengths of physics-based models with machine learning, to formulate and  
76 train ROMs for parametrized non-linear dynamical systems. A physics-based component,  
77 termed the RPM, is composed of: (1) a *lumped capacitance model* (LCM) to model the  
78 heat transfer within the TPS layers, and (2) a *surface recession model* (SRM) to model  
79 one-dimensional surface ablation.

80 Leveraging the *Mori-Zwanzig* (MZ) formalism [15, 14, 13], the RPM is rigorously ex-  
81 tended with data-driven hidden dynamics to account for the missing physics in the LCM,  
82 which are learned from high-fidelity data. The hidden dynamics enables higher predictive  
83 accuracy of the PIROM when subjected to complex boundary conditions and SRM model  
84 variations. For the TPS problem, the MZ approach produces a sufficiently simple model  
85 form while maintaining the physical consistency of the PIROM, as well as the dependence  
86 on design parameters. Thus the approach aims to solve the ITM by leveraging the gen-  
87 eralizability and computational efficiency of RPMs, while incorporating the accuracy and  
88 adaptability of data-driven extensions. More importantly, the PIROM formulation provides  
89 a general methodology for developing PIROMs for other problems.

90 The specific objectives of this work are summarized as follows:

- 91 1. Extend the previous PIROM formulation in Ref. [17] to model transient thermo-  
92 ablative response of multi-layered hypersonic TPS through a systematic coarse-graining  
93 procedure based on the Mori-Zwanzig formalism.
- 94 2. Benchmark the accuracy, generalizability, and computational accelerations of the PIROM  
95 against the RPM and the high-fidelity FEM solutions of ablating TPS, thus quanti-  
96 fying the PIROM’s capabilities to solve the ITM in complex multi-physical non-linear  
97 dynamical systems.

## 98 2 Modeling of Thermal Protection Systems

99 This section presents the problem of thermo-ablative modeling for a non-decomposing ab-  
100 lating TPS, subjected to extreme hypersonic heating. Two different but mathematically  
101 connected solution strategies are provided: (1) a high-fidelity full-order model (FOM) based  
102 on a finite element method (FEM), and (2) a low-fidelity reduced-physics model (RPM)  
103 based on a lumped capacitance model (LCM) and a one-dimensional surface velocity model  
104 (SRM). The FOM is computationally expensive but provides the highest fidelity, while the  
105 RPM is computationally efficient but has low predictive fidelity; both models are amenable to  
106 high-dimensional design variables. The RPM is used in the subsequent sections for deriving  
107 the PIROM.

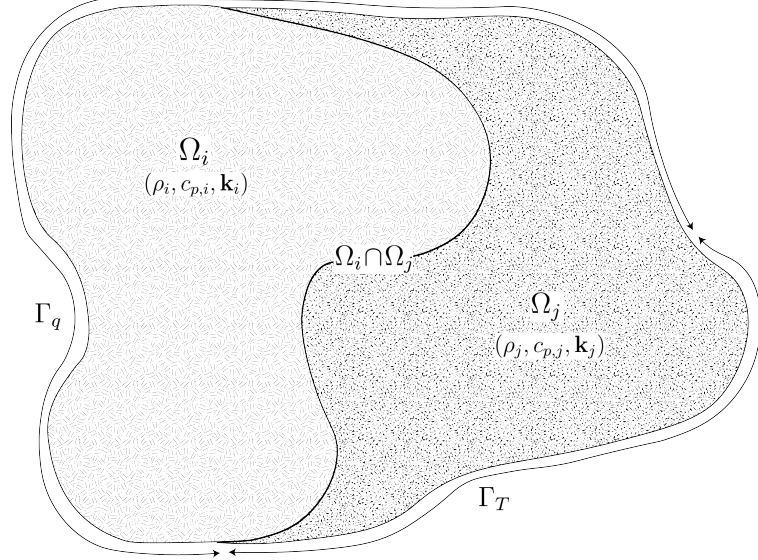


Figure 2: General domain  $\Omega$  with prescribed Neumann and Dirichlet boundary conditions on  $\Gamma_q$  and  $\Gamma_T$ . Mesh displacement  $w(x, t)$  occurs on the  $\Gamma_q$  boundary.

## 108 2.1 Governing Equations

109 The multi-physics for a non-decomposing ablating TPS involves the *energy equation* which  
 110 models the transient heat conduction inside the TPS, and the *pseudo-elasticity equation*,  
 111 which models the mesh motion due to surface recession. The governing PDEs for the ablating  
 112 TPS are summarized in this section.

### 113 2.1.1 Energy Equation

114 Consider a generic domain  $\Omega \subset \mathbb{R}^d$ ,  $d = 2$  or  $3$ , illustrated in Fig. 2. Let  $\partial\Omega = \Gamma_q \cup \Gamma_T$  and  
 115  $\Gamma_q \cap \Gamma_T = \emptyset$ , where a Neumann  $q_b(x, t)$  boundary condition is prescribed on the  $\Gamma_q$  boundary,  
 116 and represents the surface exposed to the hypersonic boundary layer. The Dirichlet  $T_b(x, t)$   
 117 boundary condition is prescribed on the boundary  $\Gamma_T$ . The TPS is divided into  $N$  non-  
 118 overlapping components  $\{\Omega_i\}_{i=1}^N$ , as illustrated in Fig. 2 for  $N = 2$ . The  $i$ -th component  $\Omega_i$   
 119 is associated with material properties  $(\rho_i, c_{p,i}, \mathbf{k}_i)$ , that are assumed to be continuous within  
 120 one component, and can be discontinuous across two neighboring components.

121 The transient heat conduction is described by the energy equation,

$$122 \quad \rho c_p \left( \frac{\partial T}{\partial t} + \tilde{\mathbf{v}}(x, t) \cdot \nabla T \right) - \nabla \cdot (\mathbf{k} \nabla T) = 0, \quad x \in \Omega \quad (1a)$$

$$- \mathbf{k} \nabla T \cdot \mathbf{n} = q_b(x, t), \quad x \in \Gamma_q \quad (1b)$$

$$T(x, t) = T_b(x, t), \quad x \in \Gamma_T \quad (1c)$$

$$T(x, 0) = T_0(x), \quad x \in \Omega \quad (1d)$$

122 where the density  $\rho$  is constant, while the heat capacity  $c_p$  and thermal conductivity  $\mathbf{k} \in \mathbb{R}^{d \times d}$   
 123 may depend on temperature. In the order they appear, the terms in eq. (1a) include, the

<sup>124</sup> unsteady energy storage, heat conduction, temperature advection due to mesh motion, and  
<sup>125</sup> source terms due to boundary conditions. The boundary conditions for the energy equation  
<sup>126</sup> includes Neumann eq. (1b) and Dirichlet eq. (1c) on  $\Gamma_T$ .

<sup>127</sup> An Arbitrary Lagrangian-Eulerian (ALE) description is used to account for mesh motion  
<sup>128</sup> due to surface recession, where  $\tilde{\mathbf{v}}(x, t)$  is the relative velocity of the material with respect to  
<sup>129</sup> the mesh,

$$\tilde{\mathbf{v}}(x, t) = \mathbf{v}_s(x, t) - \mathbf{v}_m(x, t) \quad (2)$$

<sup>130</sup> where  $\mathbf{v}_s(x, t)$  and  $\mathbf{v}_m(x, t)$  are the physical material velocity and mesh velocity, respectively.  
<sup>131</sup> In this work, the physical material velocity is assumed to be zero, i.e.,  $\mathbf{v}_s(x, t) = \mathbf{0}$ , and thus  
<sup>132</sup> the relative velocity is simply the negative of the mesh velocity,  $\tilde{\mathbf{v}}(x, t) = -\mathbf{v}_m(x, t)$ .

### <sup>133</sup> 2.1.2 Pseudo-Elasticity Equation

<sup>134</sup> The mesh motion is described by the steady-state pseudo-elasticity equation without body  
<sup>135</sup> forces,

$$\nabla \cdot \boldsymbol{\sigma}(\mathbf{w}) = \mathbf{0}, \quad \forall t \in \mathcal{T}, \mathbf{x} \in \Omega \quad (3a)$$

$$\mathbf{w}(\mathbf{x}, t) = \mathbf{w}_q(\mathbf{x}, t), \quad \forall t \in \mathcal{T}, \mathbf{x} \in \Gamma_q \quad (3b)$$

$$\mathbf{w}(\mathbf{x}, t) = \mathbf{0}, \quad \forall t \in \mathcal{T}, \mathbf{x} \notin \Gamma_q \quad (3c)$$

$$\mathbf{w}(\mathbf{x}, 0) = \mathbf{0}, \quad \forall \mathbf{x} \in \Omega \quad (3d)$$

<sup>136</sup> where the stress tensor  $\boldsymbol{\sigma}$  is related to the strain tensor  $\boldsymbol{\epsilon}(\mathbf{w})$  through Hooke's law,

$$\boldsymbol{\sigma}(\mathbf{w}) = \mathbb{D} : \boldsymbol{\epsilon}(\mathbf{w})$$

<sup>137</sup> where  $\mathbb{D}$  is the fourth-order positive definite elasticity tensor, and “ $:$ ” is the double con-  
<sup>138</sup> traction of the full-order tensor  $\mathbb{D}$  with the second-order tensor  $\boldsymbol{\epsilon}$ . The elasticity tensor  
<sup>139</sup> ordinarily possess a number of symmetries, effectively reducing the number of components  
<sup>140</sup> that describe it [2]. The symmetric strain tensor  $\boldsymbol{\epsilon}$  measures the deformation of the mesh  
<sup>141</sup> due to displacements  $\mathbf{w}(x, t)$ , and is defined as,

$$\boldsymbol{\epsilon}(\mathbf{w}) = \frac{1}{2} (\nabla \mathbf{w} + \nabla \mathbf{w}^\top)$$

<sup>142</sup> The “material” properties for the mesh are chosen to tailor the mesh deformation, and need  
<sup>143</sup> not represent the actual material being modeled [1].

<sup>144</sup> For the pseudo-elasticity equations, the boundary conditions include prescribed displace-  
<sup>145</sup> ments  $\mathbf{w}_q(x, t)$  on the heated boundary  $\Gamma_q$  in eq. (3b), and zero displacements on the unheated  
<sup>146</sup> boundaries in eq. (3c). The initial condition for the mesh displacements is zero in eq. (3d).  
<sup>147</sup> Particularly, the surface velocity due to the ablating material is a function of the surface  
<sup>148</sup> temperature  $T_q(x, t)$  for  $x \in \Gamma_q$  on the heated boundary. For the  $i$ -th material component,  
<sup>149</sup> the mesh velocity on the heated boundary is imposed based on the following relation,

$$\hat{\mathbf{n}} \cdot \mathbf{v}_m(x, t) = f(T_q(x, t)), \quad x \in \Gamma_q \quad (4)$$

<sup>150</sup> where  $\hat{\mathbf{n}}$  is the unit normal vector on the heated boundary  $\Gamma_q$ , and  $f$  is a function obtained

from tabulated data for the material, commonly referred to as a B' table [1]. The B' table provides a model for the recession velocity as a function of the surface temperature, and is pre-computed based on high-fidelity simulations of the ablation process for a one-dimensional slab of the material, and is independent of the TPS geometry. Provided the surface velocity, the boundary condition in eq. (5) for the mesh displacements are computed by integrating the surface velocity over time,

$$\mathbf{w}_q(x, t) = \int_0^t \mathbf{v}_m(x, \tau) d\tau \quad (5)$$

## 2.2 Full-Order Model: Finite-Element Method

To obtain the full-order numerical solution, the *energy equation* is spatially discretized using variational principles of the Discontinuous Galerkin (DG) method [5]. Note that the choice of DG approach is mainly for theoretical convenience, and is exclusively performed on the energy equation, as it is the surface temperature that drives the ablation process. The equivalence between DG and FEM is noted upon their convergence. For the *pseudo-elasticity equation* standard FEM is used to compute the mesh displacements based on the surface temperature provided by the DG solution of the energy equation [2].

Consider a conforming mesh partition domain, where each element belongs to one and only one component. Denote the collection of all  $M$  elements as  $\{E_i\}_{i=1}^M$ . In an element  $E_i$ , its shared boundaries with another element  $E_j$ , Neumann BC, and Dirichlet BC are denoted as  $e_{ij}$ ,  $e_{iq}$ , and  $e_{iT}$ , respectively. Lastly,  $|e|$  denotes the length ( $n_d = 2$ ) or area ( $n_d = 3$ ) of a component boundary  $e$ . For the  $i$ -th element, use a set of  $P$  trial functions, such as polynomials, to represent the temperature distribution,

$$T_i(x, t) = \sum_{l=1}^P \phi_l^i(x) u_l^i(t) \equiv \boldsymbol{\phi}_i^\top(x) \mathbf{u}_i(t), \quad i = 1, 2, \dots, M \quad (6)$$

Without loss of generality, the trial functions are assumed to be orthogonal, so that,

$$\int_{E_i} \phi_l^i(x) \phi_k^i(x) d\Omega = 0, \quad l \neq k$$

where  $\delta_{lk}$  is the Kronecker delta function. Furthermore, for simplicity, choose  $\phi_1^i = 1$ . Thus, by orthogonality,

$$\int_{E_i} \phi_1^i(x) d\Omega = |E_i|, \quad \int_{E_i} \phi_k^i(x) d\Omega = 0, \quad k = 2, 3, \dots, P$$

Under the choice of basis functions,  $u_1^i$  is simply the average temperature of element  $E_i$ , denoted as  $\bar{u}_i$ .

By standard variational processes, e.g., [5], the element-wise governing equation is de-

<sup>177</sup> noted as,

$$\mathbf{A}_i \dot{\mathbf{u}}_i = (\mathbf{B}_i + \mathbf{C}_i) \mathbf{u}_i + \sum_{j \in \mathcal{N}_i \cup \{T_b\}} (\mathbf{B}_{ij}^i \mathbf{u}_i + \mathbf{B}_{ij}^j \mathbf{u}_j) + \mathbf{f}_i(t), \quad \text{for } i = 1, 2, \dots, M \quad (7)$$

<sup>178</sup> which is collected as the following ODE for all the elements in the mesh,

$$\mathbf{A}(\mathbf{u}) \dot{\mathbf{u}} = [\mathbf{B}(\mathbf{u}) + \mathbf{C}(\mathbf{u})] \mathbf{u} + \mathbf{f}(t) \quad (8)$$

<sup>179</sup> where  $\mathbf{u} = [\mathbf{u}_1, \mathbf{u}_2, \dots, \mathbf{u}_M]^T \in \mathbb{R}^{MP}$  includes all the DG variables,  $\mathbf{f} \in \mathbb{R}^{MP}$  is the external forcing, and the system matrices  $\mathbf{A}$ ,  $\mathbf{B}$ , and  $\mathbf{C}$  are the matrices due to heat capacity, heat conduction, and temperature advection due to mesh motion, respectively. A detailed derivation of eqs. (7) and (8) and their matrices is provided in Appendix A.

### <sup>183</sup> 2.3 Reduced-Physics Model

<sup>184</sup> The RPM for predicting the response of the ablating TPS consists of two components: (1) the *lumped-capacitance model* (LCM), and (2) the *surface recession model* (SRM). The LCM is described as a first-order system of ODEs for predicting the average temperatures inside the components of the TPS, and provides a low-fidelity (under estimate) for the component's surface temperature. The SRM provides a relation between the surface temperature and the surface recession velocity based on pre-computed B' tables for the material, enabling the computation of one-dimensional surface displacements. The LCM and SRM are combined to define the RPM, providing low-fidelity estimates for the temperatures and surface recession of the ablating TPS.

#### <sup>193</sup> 2.3.1 Lumped Capacitance Model

<sup>194</sup> A general form of the LCM is provided in this section; details regarding the derivation for the four-component TPS used in the results section are provided in Appendix A. The LCM is a classical physics-based low-order model for predicting the temporal variation of average temperature in multiple interconnected components [9]. The LCM is derived at the component level from a point of view of energy conservation, and leads to the following system of ODEs for the average temperatures on the components,

$$\bar{\mathbf{A}} \dot{\bar{\mathbf{u}}} = \bar{\mathbf{B}} \bar{\mathbf{u}} + \bar{\mathbf{f}}(t) \quad (9)$$

<sup>200</sup> Where the states and inputs,

$$\bar{\mathbf{u}} = [\bar{u}_1, \bar{u}_2, \dots, \bar{u}_N]^T \in \mathbb{R}^N, \quad \bar{\mathbf{f}} = [\bar{f}_1, \bar{f}_2, \dots, \bar{f}_N]^T \in \mathbb{R}^N \quad (10)$$

<sup>201</sup> include the average temperatures  $\bar{\mathbf{u}}$  and spatially-integrated inputs  $\bar{\mathbf{f}}$  for the  $N$  components.  
<sup>202</sup> For  $i, j = 1, 2, \dots, N$  the  $(i, j)$ -th elements of the  $\bar{\mathbf{A}} \in \mathbb{R}^{N \times N}$ ,  $\bar{\mathbf{B}} \in \mathbb{R}^{N \times N}$ , and  $\bar{\mathbf{f}} \in \mathbb{R}^N$

203 matrices are given by,

$$\bar{A}_i = \begin{cases} \int_{\Omega_i} \rho c_p d\Omega_i, & i = j \\ 0, & i \neq j \end{cases}, \quad \bar{B}_{ij} = \begin{cases} \sum_{j \in \mathcal{N}_i \cup \{T_b\}} \bar{B}_{ij}^i, & i = j \\ \bar{B}_{ij}^{(j)}, & i \neq j \end{cases}, \quad (11a)$$

$$\mathbf{f}_i = \begin{cases} |e_{iq}| \bar{q}_i + \frac{|e_{iT}|}{R_i} \bar{T}_i, & i = j \\ 0, & i \neq j \end{cases} \quad (11b)$$

204 where,

$$\bar{q}_i = \frac{1}{|e_{iq}|} \int_{e_{iq}} q_b d e_{iq}, \quad \bar{T}_i = \frac{1}{|e_{iT}|} \int_{e_{iT}} T_b d e_{iT}, \quad \bar{B}_{ij}^i = -\frac{|e_{ij}|}{R_{ij}}, \quad \bar{B}_{ij}^j = \frac{|e_{ij}|}{R_{ij}} \quad (12)$$

205 where  $R_{ij}$  is the equivalent thermal resistance between two neighboring components  $\Omega_i$  and  
206  $\Omega_j$ , and  $R_i$  is the thermal resistance between component  $\Omega_i$  and the Dirichlet boundary.  
207 The thermal resistances are computed based on the geometry and material properties of the  
208 components; details regarding their computation are provided in Appendix A.

### 209 2.3.2 Surface Recession Model

210 The displacement is assumed to be *one-dimensional* on the heated boundary  $\Gamma_q$ , i.e., the  
211 surface recedes only in the direction of the applied load. Displacements perpendicular to  
212 the direction of the applied load are assumed small and are neglected. Thus, for the  $i$ -th  
213 ablating component, the one-dimensional SRM considered in this work takes the form,

$$\dot{\mathbf{w}} = \boldsymbol{\Xi} \bar{\mathbf{u}} - \tilde{\mathbf{f}} \quad (13)$$

214 where  $\boldsymbol{\Xi} = \text{diag}(\alpha_1, \dots, \alpha_{\tilde{N}})$  and  $\tilde{\mathbf{f}} = (\alpha_1 \bar{u}_{0,1}, \dots, \alpha_{\tilde{N}} \bar{u}_{0,\tilde{N}})^\top$ . The constants  $\alpha_i$  are small  
215 material-dependent constants, determined from the B' table, and  $\bar{u}_{0,i}$  is the constant initial  
216 temperature of the ablative component. The SRM provides a relation between the surface's  
217 temperature and recession velocity, based on pre-computed B' tables for the material.

### 218 2.3.3 Thermo-Ablative Reduced-Physics Model

219 The LCM and SRM are combined to define the RPM for predicting the thermo-ablative  
220 response of the TPS under hypersonic boundary layers. Specifically, the RPM is defined as  
221 the LCM as in eq. (9), where the *geometry- and temperature-dependent matrices*  $\bar{\mathbf{A}}$ ,  $\bar{\mathbf{B}}$ , and  
222  $\tilde{\mathbf{f}}$  are updated at each time step based on the current temperature  $\bar{\mathbf{u}}$  and displacements  $\mathbf{w}$   
223 provided by the SRM. The RPM is formally stated as,

$$\tilde{\mathbf{A}}(\mathbf{s}) \dot{\mathbf{s}} = \tilde{\mathbf{B}}(\mathbf{s}) \mathbf{s} + \tilde{\mathbf{F}}(t) \quad (14a)$$

$$\tilde{\mathbf{z}} = \mathbf{I} \mathbf{s} \quad (14b)$$

224 where the state  $\mathbf{s} = [\bar{\mathbf{u}}, \mathbf{w}]^\top \in \mathbb{R}^{N+\tilde{N}}$  includes the *average temperature* and *one-dimensional*  
225 *surface displacements*, and  $\tilde{N}$  is the number of ablating components with  $\tilde{N} \leq N$ . Moreover,

226 the observables are defined as  $\mathbf{z} = [\bar{\mathbf{u}}, \mathbf{w}]^\top \in \mathbb{R}^{N+\tilde{N}}$ . The matrices are given as,

$$\tilde{\mathbf{A}}(\mathbf{s}) = \begin{bmatrix} \bar{\mathbf{A}}(\mathbf{s}) & \mathbf{0} \\ \mathbf{0} & \mathbf{I} \end{bmatrix}, \quad \tilde{\mathbf{B}}(\mathbf{s}) = \begin{bmatrix} \bar{\mathbf{B}}(\mathbf{s}) & \mathbf{0} \\ \boldsymbol{\Xi} & \mathbf{0} \end{bmatrix}, \quad \tilde{\mathbf{F}}(t) = \begin{bmatrix} \bar{\mathbf{f}}(t) \\ -\tilde{\mathbf{f}} \end{bmatrix} \quad (15)$$

227 In the matrices  $\tilde{\mathbf{A}}$  and  $\tilde{\mathbf{B}}$ , the surface displacements  $\mathbf{w}$  are used to define the dimensions for  
228 the  $\Omega_i$  component used in eqs. (11) and (12), thus effectively coupling the LCM and SRM.

## 229 2.4 Summary of Modeling Approaches

230 The FOM (i.e., FEM) and RPM (i.e., LCM with SRM) are two different but mathemati-  
231 cally connected solution strategies. Particularly, the LCM in eq. (9) not only resembles the  
232 functional form of the DG model in eq. (8), but can be viewed as a special case of the latter,  
233 where the mesh partition is extremely coarse, and the trial and test functions are piece-wise  
234 constants. This removes all spatial variations within each component, and neglects advection  
235 effects due to mesh motion.

236 For example, consider the case where each component  $\Omega_i$  is treated as one single element,  
237 and each element employs one constant basis function  $\phi_i = 1$ . The element-wise DG model  
238 in eq. (7) simplifies into a scalar ODE,

$$\mathbf{A}^{(i)} = \bar{A}_i, \quad \mathbf{C}^{(i)} = 0, \quad \mathbf{B}_{ij}^{(i)} = -\sigma|e_{ij}|, \quad \mathbf{B}_{ij}^{(j)} = \sigma|e_{ij}|, \quad \mathbf{f}_i = |e_{iq}|\bar{q}_i + \sigma|e_{iT}|\bar{T}_i \quad (16)$$

239 Clearly, the LCM is a coarse zeroth-order DG model with the inverse of thermal resistance  
240 chosen as the element-wise penalty factors. Or conversely, the DG model is a refined version  
241 of LCM via *hp*-adaptation.

242 The FOM and RPM represent two extremes in the modeling fidelity and computational  
243 cost spectrum. On one hand, the FOM is the most accurate but computationally expensive  
244 to evaluate due to the fine mesh discretizations for both the temperature and displacement  
245 fields, leading to possibly millions of state variables. On the other hand, the RPM consid-  
246 ers only the average temperature of the material, from which the one-dimensional surface  
247 displacements are computed by integrating eq. (13). This considerably reduces the com-  
248 putational cost, but sacrifices local temperature information that are critical to properly  
249 capture higher-order effects due to mesh motion and thermal gradients within each compo-  
250 nent. Thus, neither the FOM nor the RPM is an universal approach for real-world analysis,  
251 design, and optimization tasks for ablating TPS, where thousands of high-fidelity model  
252 evaluations may be necessary. This issue motivates the development of the PIROM, which  
253 can achieve the fidelity of FOM at a computational cost close to the RPM, while maintaining  
254 the generalizability to model parameters.

## 255 3 Physics-Infused Reduced-Order Modeling

256 The formulation of PIROM for ablating TPS starts by connecting the FOM, i.e., the DG-  
257 FEM, and the RPM, i.e., the LCM, via a coarse-graining procedure. This procedure pin-  
258 points the missing dynamics in the LCM when compared to DG-FEM. Subsequently, the

259 Mori-Zwanzig (MZ) formalism is employed to determine the model form for the missing dy-  
260 namics in PIROM. Lastly, the data-driven identification of the missing dynamics in PIROM  
261 is presented.

### 262 3.1 Deriving the Reduced-Physics Model via Coarse-Graining

263 The subsequent coarse-graining formulation is performed on the DG-FEM in eq. (8) to derive  
264 the LCM in eq. (9). This process constraints the trial function space of a full-order DG model  
265 to a subset of piece-wise constants, so that the variables  $\mathbf{u}$ , matrices  $\mathbf{A}$ ,  $\mathbf{B}$ , and  $\mathbf{C}$ , and forcing  
266 vector  $\mathbf{f}$  are all approximated using a single state associated to the average temperature.  
267 Note that the coarse-graining is exclusively performed on the thermal dynamics, as it is  
268 the surface temperature that drives the one-dimensional recession via the SRM. Hence, the  
269 coarse-graining of the mesh dynamics is not included in the following procedure.

#### 270 3.1.1 Coarse-Graining of States

271 Consider a DG model as in eq. (8) for  $M$  elements and an LCM as in eq. (9) for  $N$  components;  
272 clearly  $M \gg N$ . Let  $\mathcal{V}_j = \{i | E_i \in \Omega_j\}$  be the indices of the elements belonging to the  $j$ -th  
273 component, so  $E_i \in \Omega_j$  for all  $i \in \mathcal{V}_j$ . The number of elements in the  $j$ -th component is  $|\mathcal{V}_j|$ .  
274 The average temperature on  $\Omega_j$  is,

$$\bar{u}_j = \frac{1}{|\Omega_j|} \sum_{i \in \mathcal{V}_j} \int_{E^{(i)}} \boldsymbol{\phi}^{(i)}(x)^T \mathbf{u}^{(i)} d\Omega = \frac{1}{|\Omega_j|} \sum_{i \in \mathcal{V}_j} |E_i| \boldsymbol{\varphi}_i^{j\top} \mathbf{u}^{(i)}, \quad j = 1, 2, \dots, N \quad (17)$$

275 where  $|\Omega_j|$  and  $|E_i|$  denote the area ( $d = 2$ ) or volume ( $d = 3$ ) of component  $j$  and element  
276  $i$ , respectively. The orthogonal basis functions are defined as  $\boldsymbol{\varphi}_i^{j\top} = [1, 0, \dots, 0]^\top \in \mathbb{R}^P$ .

277 Conversely, given the average temperatures of the  $N$  components,  $\bar{\mathbf{u}}$ , the states of an  
278 arbitrary element  $E_i$  is written as,

$$\mathbf{u}^{(i)} = \sum_{k=1}^N \boldsymbol{\varphi}_i^k \bar{u}_k + \delta \mathbf{u}^{(i)}, \quad i = 1, 2, \dots, M \quad (18)$$

279 where  $\boldsymbol{\varphi}_i^k = 0$  if  $i \notin \mathcal{V}_k$ , and  $\delta \mathbf{u}^{(i)}$  represents the deviation from the average temperature and  
280 satisfies the orthogonality condition  $\boldsymbol{\varphi}_i^{k\top} \delta \mathbf{u}^{(i)} = 0$  for all  $k$ .

281 Equations eqs. (17) and (18) are combined and written in matrix form as,

$$\bar{\mathbf{u}} = \boldsymbol{\Phi}^+ \mathbf{u}, \quad \mathbf{u} = \boldsymbol{\Phi} \mathbf{u} + \delta \mathbf{u} \quad (19)$$

282 where  $\boldsymbol{\Phi} \in \mathbb{R}^{MP \times N}$  is a matrix of  $M \times N$  blocks, with the  $(i, j)$ -th block as  $\boldsymbol{\varphi}_i^j$ ,  $\boldsymbol{\Phi}^+ \in \mathbb{R}^{N \times MP}$   
283 is the left inverse of  $\boldsymbol{\Phi}$ , with the  $(i, j)$ -th block as  $\boldsymbol{\varphi}_i^{j+} = \frac{|E_i|}{|\Omega_j|} \boldsymbol{\varphi}_i^{j\top}$ , and  $\delta \mathbf{u}$  is the collection of  
284 deviations. By their definitions,  $\boldsymbol{\Phi}^+ \boldsymbol{\Phi} = \mathbf{I}$  and  $\boldsymbol{\Phi}^+ \delta \mathbf{u} = \mathbf{0}$ .

285 **3.1.2 Coarse-Graining of Dynamics**

286 The dependence of the matrices with respect to the displacements  $\mathbf{w}$  is dropped to isolate  
 287 the analysis based on coarsened variables. Consider a function of states in the form of  
 288  $\mathbf{M}(\mathbf{u})\mathbf{g}(\mathbf{u})$ , where  $\mathbf{g} : \mathbb{R}^{MP} \rightarrow \mathbb{R}^{MP}$  is a vector-valued function, and  $\mathbf{M} : \mathbb{R}^{MP} \rightarrow \mathbb{R}^{p \times MP}$   
 289 is a matrix-valued function with an arbitrary dimension  $p$ . Define the projection matrix  
 290  $\mathbf{P} = \Phi\Phi^+$  and the projection operator  $\mathcal{P}$  as,

$$\begin{aligned}\mathcal{P}[\mathbf{M}(\mathbf{u})\mathbf{g}(\mathbf{u})] &= \mathbf{M}(\mathbf{Pu})\mathbf{g}(\mathbf{Pu}) \\ &= \mathbf{M}(\Phi\bar{\mathbf{u}})\mathbf{g}(\Phi\bar{\mathbf{u}})\end{aligned}\quad (20)$$

291 so that the resulting function depends only on the average temperatures  $\bar{\mathbf{u}}$ . Correspondingly,  
 292 the residual operator  $\mathcal{Q} = \mathcal{I} - \mathcal{P}$ , and  $\mathcal{Q}[\mathbf{M}(\mathbf{u})\mathbf{g}(\mathbf{u})] = \mathbf{M}(\mathbf{u})\mathbf{g}(\mathbf{u}) - \mathbf{M}(\Phi\bar{\mathbf{u}})\mathbf{g}(\Phi\bar{\mathbf{u}})$ . When  
 293 the function is not separable, the projection operator is simply defined as  $\mathcal{P}[\mathbf{g}(\mathbf{u})] = \mathbf{g}(\mathbf{Pu})$ .

294 Subsequently, the operators defined above are applied to coarse-grain the dynamics. First,  
 295 write the DG-FEM in eq. (8) as,

$$\dot{\mathbf{u}} = \mathbf{A}(\mathbf{u})^{-1}\mathbf{B}(\mathbf{u})\mathbf{u} + \mathbf{A}(\mathbf{u})^{-1}\mathbf{C}(\mathbf{u})\mathbf{u} + \mathbf{A}(\mathbf{u})^{-1}\mathbf{f}(t) \quad (21)$$

296 and multiply both sides by  $\Phi^+$  to obtain,

$$\Phi^+\dot{\mathbf{u}} = \Phi^+(\Phi\dot{\bar{\mathbf{u}}} + \delta\dot{\mathbf{u}}) = \dot{\bar{\mathbf{u}}} = \Phi^+\mathbf{r}(\mathbf{u}, t) \quad (22)$$

297 Apply the projection operator  $\mathcal{P}$  and the residual operator  $\mathcal{Q}$  to the right-hand side to obtain,

$$\dot{\bar{\mathbf{u}}} = \mathcal{P}[\Phi^+\mathbf{r}(\mathbf{u}, t)] + \mathcal{Q}[\Phi^+\mathbf{r}(\mathbf{u}, t)] \equiv \mathbf{r}^{(1)}(\mathbf{u}, t) + \mathbf{r}^{(2)}(\mathbf{u}, t) \quad (23)$$

298 where  $\mathbf{r}^{(1)}(\mathbf{u}, t)$  is resolved dynamics that depends on  $\bar{\mathbf{u}}$  only, and  $\mathbf{r}^{(2)}(\mathbf{u}, t)$  is the un-resolved  
 299 or residual dynamics. Detailed derivations and analysis of  $\mathbf{r}^{(1)}(\mathbf{u}, t)$  and  $\mathbf{r}^{(2)}(\mathbf{u}, t)$  can be  
 300 found in the Appendix.

301 It follows from Ref. [17] that the resolved dynamics is exactly the LCM, where the  
 302 advection term reduces to zero, i.e.,  $\bar{\mathbf{C}}(\bar{\mathbf{u}}) = \mathbf{0}$  as shown in the Appendix. Using the notation  
 303 from eq. (9), it follows that,

$$\begin{aligned}\mathbf{r}^{(1)}(\mathbf{u}, t) &= \bar{\mathbf{A}}(\bar{\mathbf{u}})^{-1}\bar{\mathbf{B}}(\bar{\mathbf{u}})\bar{\mathbf{u}} + \bar{\mathbf{A}}(\bar{\mathbf{u}})^{-1}\bar{\mathbf{C}}(\bar{\mathbf{u}})\bar{\mathbf{u}} + \bar{\mathbf{A}}(\bar{\mathbf{u}})^{-1}\bar{\mathbf{f}}(\bar{\mathbf{u}}) \\ &= \bar{\mathbf{A}}(\bar{\mathbf{u}})^{-1}\bar{\mathbf{B}}(\bar{\mathbf{u}})\bar{\mathbf{u}} + \bar{\mathbf{A}}(\bar{\mathbf{u}})^{-1}\bar{\mathbf{f}}(t)\end{aligned}\quad (24)$$

304 where the following relations hold,

$$\bar{\mathbf{A}}(\bar{\mathbf{u}}) = \mathbf{W}(\Phi^+\mathbf{A}(\Phi\bar{\mathbf{u}})^{-1}\Phi)^{-1} \quad (25a)$$

$$\bar{\mathbf{B}}(\bar{\mathbf{u}}) = \mathbf{W}\Phi^+\mathbf{B}(\Phi\bar{\mathbf{u}})\Phi \quad (25b)$$

305 where  $\mathbf{W} \in \mathbb{R}^{N \times N}$  is a diagonal matrix with the  $i$ -th element as  $[\mathbf{W}]_{ii} = |\mathcal{V}_k|$  if  $i \in \mathcal{V}_k$ .

306 The examination of the second residual term  $\mathbf{r}^{(2)}(\mathbf{u}, t)$  in eq. (23) is shown in the Appendix,  
 307 and demonstrates that the physical sources of missing dynamics in the LCM include: the  
 308 approximation of non-uniform temperature within each component as a constant, and the

309 elimination of the advection term due to coarse-graining. In sum, the above results not  
 310 only show that the LCM is a result of coarse-graining of the full-order DG-FEM, but also  
 311 reveal the discrepancies between the LCM and the DG-FEM. These discrepancies propagate  
 312 into the SRM, which as a result of the averaging in the LCM formulation, under-predicts  
 313 the surface recession rates. In the subsequent section, the discrepancies in the LCM are  
 314 corrected to formulate the PIROM.

### 315 3.2 Physics-Infusion Via Mori-Zwanzig Formalism

316 The Mori-Zwanzig (MZ) formalism is an operator-projection technique used to derive ROMs  
 317 for high-dimensional dynamical systems, especially in statistical mechanics and fluid dy-  
 318 namics [13, 14, 15]. It provides an exact reformulation of a high-dimensional Markovian dy-  
 319 namical system, into a low-dimensional observable non-Markovian dynamical system. The  
 320 proposed ROM is subsequently developed based on the approximation to the non-Markovian  
 321 term in the observable dynamics. Particularly, eq. (23) shows that the DG-FEM dyna-  
 322 mics can be decomposed into the resolved dynamics  $\mathbf{r}^{(1)}(\bar{\mathbf{u}}, t)$  and the orthogonal dynamics  
 323  $\mathbf{r}^{(2)}(\bar{\mathbf{u}}, t)$ , in the sense of  $\mathcal{P}\mathbf{r}^{(2)} = 0$ . In this case, the MZ formalism can be invoked to ex-  
 324 press the dynamics  $\dot{\bar{\mathbf{u}}}$  in terms of  $\bar{\mathbf{u}}$  alone as the projected Generalized Langevin Equation  
 325 (GLE) [13, 14, 15],

$$\dot{\bar{\mathbf{u}}}(t) = \mathbf{r}^{(1)}(\bar{\mathbf{u}}, t) + \int_0^t \tilde{\kappa}(t, s, \bar{\mathbf{u}}) ds \quad (26)$$

326 where the first and second terms are referred to as the Markovian and non-Markovian terms,  
 327 respectively. The non-Markovian term accounts for the effects of past un-resolved states on  
 328 the current resolved states via a memory kernel  $\tilde{\kappa}(t, s, \bar{\mathbf{u}})$ , which in practice is computa-  
 329 tionally expensive to evaluate.

#### 330 3.2.1 Markovian Reformulation

331 This section details the formal derivation of the PIROM as a system of ODEs for the thermal  
 332 dynamics, based on approximations to the memory kernel. Specifically, the kernel  $\tilde{\kappa}$  is  
 333 examined via a leading-order expansion, based on prior work [19]; this can be viewed as an  
 334 analog of zeroth-order holding in linear system theory with a sufficiently small time step. In  
 335 this case, the memory kernel is approximated as,

$$\tilde{\kappa}(t, s, \bar{\mathbf{u}}) \approx \mathbf{r}^{(1)}(\bar{\mathbf{u}}, t) \cdot \nabla_{\bar{\mathbf{u}}} \mathbf{r}^{(2)}(\Phi \bar{\mathbf{u}}, t) \quad (27)$$

336 Note that the terms in  $\mathbf{r}^{(1)}$  have a common factor  $\bar{\mathbf{A}}^{-1}$ ; this motivates the following heuristic  
 337 modification of the model form in eq. (26),

$$\dot{\bar{\mathbf{u}}} = \mathbf{r}^{(1)}(\bar{\mathbf{u}}, t) + \bar{\mathbf{A}}^{-1}(\bar{\mathbf{u}}) \int_0^t \kappa(t, s, \bar{\mathbf{u}}) ds \quad (28a)$$

$$\bar{\mathbf{A}}(\bar{\mathbf{u}}) \dot{\bar{\mathbf{u}}} = \bar{\mathbf{B}}(\bar{\mathbf{u}}) \bar{\mathbf{u}} + \bar{\mathbf{f}}(t) + \int_0^t \kappa(t, s, \bar{\mathbf{u}}) ds \quad (28b)$$

338 where the original kernel  $\tilde{\kappa}$  is effectively normalized by  $\bar{\mathbf{A}}^{-1}$ . Intuitively, such choice of kernel  
 339 reduces its dependency on the averaged material properties, and simplifies the subsequent  
 340 design of model form.

341 Subsequently, the hidden states are introduced to “Markovianize” the system eq. (26).  
 342 In this manner, eq. (28b) is converted into a pure state-space model, with the functional  
 343 form of the LCM retained; since LCM is a physics-based model, then it encodes the phys-  
 344 ical information and retains explicit parametric dependence of the problem. Consider the  
 345 representation of the kernel as a finite sum of simpler functions, e.g., exponentials,

$$\kappa(t, s, \bar{\mathbf{u}}) = \sum_{j=1}^m \mathcal{K}_j(t, s, \bar{\mathbf{u}}) [\mathbf{p}_j + \mathbf{d}_j(\bar{\mathbf{u}})] \phi_j(s, \bar{\mathbf{u}}) \quad (29)$$

346 where,

$$\mathcal{K}_j(t, s, \bar{\mathbf{u}}) = e^{-\int_s^t (\lambda_j + e_j(\bar{\mathbf{u}})) d\tau}, \quad \phi_j(s, \bar{\mathbf{u}}) = \mathbf{q}_j^\top \bar{\mathbf{u}}(s) + \mathbf{g}_j(\bar{\mathbf{u}})^\top \bar{\mathbf{u}}(s) + \mathbf{r}_j^\top \bar{\mathbf{f}}(s) \quad (30)$$

347 with suitable coefficients  $\mathbf{p}_j, \mathbf{d}_j, \mathbf{q}_j, \mathbf{g}_j, \mathbf{r}_j \in \mathbb{R}^N$  and decay rates  $\lambda_j, e_j(\bar{\mathbf{u}}) > 0$ , that need to  
 348 be identified from data.

349 Define the hidden states as,

$$\beta_j(t) = \int_0^t \mathcal{K}_j(s, \bar{\mathbf{u}}) \phi_j(s, \bar{\mathbf{u}}) ds \quad (31)$$

350 and differentiate with respect to time,,

$$\dot{\beta}_j(t) = -[\lambda_j + e_j(\bar{\mathbf{u}})] \beta_j(t) + \mathbf{q}_j^\top \bar{\mathbf{u}}(t) + \mathbf{g}_j(\bar{\mathbf{u}})^\top \bar{\mathbf{u}}(t) + \mathbf{r}_j^\top \bar{\mathbf{f}}(t) \quad (32)$$

351 to obtain the memory,

$$\int_0^t \kappa(t, s, \bar{\mathbf{u}}) ds = \sum_{j=1}^m [\mathbf{p}_j + \mathbf{d}_j(\bar{\mathbf{u}})] \beta_j(t) \quad (33)$$

352 Then, eq. (28b) is recast as the extended Markovian system,

$$\bar{\mathbf{A}}(\bar{\mathbf{u}}) \dot{\bar{\mathbf{u}}} = \bar{\mathbf{B}}(\bar{\mathbf{u}}) \bar{\mathbf{u}} + [\mathbf{P} + \mathbf{D}(\bar{\mathbf{u}})] \boldsymbol{\beta} + \bar{\mathbf{f}}(t) \quad (34a)$$

$$\dot{\boldsymbol{\beta}} = [\mathbf{Q} + \mathbf{G}(\bar{\mathbf{u}})] \bar{\mathbf{u}} + [\mathbf{E}(\bar{\mathbf{u}}) - \boldsymbol{\Lambda}] \boldsymbol{\beta} + \mathbf{R} \bar{\mathbf{f}}(t) \quad (34b)$$

353 where the data-driven operators associated to the hidden dynamics are collected as,

$$\boldsymbol{\Lambda} = \text{diag}(\lambda_1, \lambda_2, \dots, \lambda_m) \in \mathbb{R}^{m \times m}, \quad \mathbf{P} = [\mathbf{p}_1, \mathbf{p}_2, \dots, \mathbf{p}_m] \in \mathbb{R}^{N \times m} \quad (35a)$$

$$\mathbf{D}(\bar{\mathbf{u}}) = [\mathbf{d}_1(\bar{\mathbf{u}}), \mathbf{d}_2(\bar{\mathbf{u}}), \dots, \mathbf{d}_m(\bar{\mathbf{u}})] \in \mathbb{R}^{N \times m}, \quad \mathbf{Q} = [\mathbf{q}_1, \mathbf{q}_2, \dots, \mathbf{q}_m] \in \mathbb{R}^{m \times N} \quad (35b)$$

$$\mathbf{G}(\bar{\mathbf{u}}) = [\mathbf{g}_1(\bar{\mathbf{u}}), \mathbf{g}_2(\bar{\mathbf{u}}), \dots, \mathbf{g}_m(\bar{\mathbf{u}})] \in \mathbb{R}^{m \times N}, \quad \mathbf{R} = [\mathbf{r}_1, \mathbf{r}_2, \dots, \mathbf{r}_m] \in \mathbb{R}^{m \times N} \quad (35c)$$

$$\mathbf{E}(\bar{\mathbf{u}}) = \text{diag}(e_1(\bar{\mathbf{u}}), e_2(\bar{\mathbf{u}}), \dots, e_m(\bar{\mathbf{u}})) \in \mathbb{R}^{m \times m} \quad (35d)$$

354 The form of the temperature-dependent matrices  $\mathbf{D}(\bar{\mathbf{u}})$ ,  $\mathbf{G}(\bar{\mathbf{u}})$ , and  $\mathbf{E}(\bar{\mathbf{u}})$  is specified in the

355 next section. Since the hidden states  $\beta$  serve as the memory, their initial conditions are set  
356 to zero, i.e.,  $\beta(t_0) = \mathbf{0}$ , no memory at the beginning. The physics-infused model in eq. (34)  
357 retains the structure of the LCM, while the hidden states account for missing physics through  
358 corrections to the stiffness and advection matrices, as well as the forcing term.

### 359 3.2.2 Coupled Physics-Infused Model

360 The next step involves coupling the physics-infused model in eq. (34) with the SRM in  
361 eq. (13) to define the PIROM for ablating TPS. To this end, define the observables as the  
362 surface temperature  $\mathbf{z}_u \in \mathbb{R}^{\tilde{N}}$  and displacements  $\mathbf{z}_w \in \mathbb{R}^{\tilde{N}}$  for  $\tilde{N} \leq N$  ablating components  
363 to define the observable vector as  $\mathbf{z} = [\mathbf{z}_u, \mathbf{z}_w]^\top \in \mathbb{R}^{n_z}$  with  $n_z = 2\tilde{N}$  as the total number of  
364 observables.

365 Collect the RPM and hidden states into a single state vector  $\mathbf{y} = [\bar{\mathbf{u}}, \mathbf{w}, \beta]^\top \in \mathbb{R}^{n_y}$ , where  
366  $n_y = N + \tilde{N} + m$ , and define a data-driven operator  $\mathbf{M} \in \mathbb{R}^{n_z \times n_y}$  to define the PIROM's  
367 observable as,

$$\mathbf{z} = \mathbf{My} \quad (36)$$

368 where,

$$\mathbf{M} = \begin{bmatrix} \mathbf{M}_{\bar{u}} & \mathbf{0} & \mathbf{M}_\beta \\ \mathbf{0} & \mathbf{I} & \mathbf{0} \end{bmatrix} \quad (37)$$

369 includes the matrices  $\mathbf{M}_{\bar{u}} \in \mathbb{R}^{\tilde{N} \times N}$  and  $\mathbf{M}_\beta \in \mathbb{R}^{\tilde{N} \times m}$ , which computes the surface tempera-  
370 ture observable from the RPM states and hidden states, respectively. The PIROM is coupled  
371 to the SRM in eq. (13) by leveraging eq. (36) to compute the surface recession velocity. Thus,  
372 the PIROM is formally stated as,

$$\mathcal{A}\dot{\mathbf{y}} = [\mathcal{B} + \mathcal{C}] \mathbf{y} + \mathcal{F}(t) \quad (38a)$$

$$\mathbf{z} = \mathbf{My} \quad (38b)$$

373 where,

$$\mathcal{A} = \begin{bmatrix} \bar{\mathbf{A}} & \mathbf{O} & \mathbf{O} \\ \mathbf{O} & \mathbf{I} & \mathbf{O} \\ \mathbf{O} & \mathbf{O} & \mathbf{I} \end{bmatrix} \in \mathbb{R}^{n_y \times n_y}, \quad \mathcal{B} = \begin{bmatrix} \bar{\mathbf{B}} & \mathbf{O} & \mathbf{P} \\ \Xi \mathbf{M}_u & \mathbf{O} & \Xi \mathbf{M}_\beta \\ \mathbf{Q} & \mathbf{O} & -\Lambda \end{bmatrix} \in \mathbb{R}^{n_y \times n_y}, \quad (39a)$$

$$\mathcal{C} = \begin{bmatrix} \mathbf{O} & \mathbf{O} & \mathbf{D}(\bar{\mathbf{u}}) \\ \mathbf{O} & \mathbf{O} & \mathbf{O} \\ \mathbf{G}(\bar{\mathbf{u}}) & \mathbf{O} & \mathbf{E}(\bar{\mathbf{u}}) \end{bmatrix} \in \mathbb{R}^{n_y \times n_y}, \quad \mathcal{F} = \begin{bmatrix} \bar{\mathbf{f}}(t) \\ -\bar{\mathbf{f}} \\ \mathbf{R}\bar{\mathbf{f}}(t) \end{bmatrix} \in \mathbb{R}^{n_y} \quad (39b)$$

374 The learnable parameters in the PIROM are collected as,

$$\Theta = \{\mathbf{P}, \mathbf{Q}, \mathbf{R}, \mathbf{D}(\bar{\mathbf{u}}), \mathbf{G}(\bar{\mathbf{u}}), \mathbf{E}(\bar{\mathbf{u}}), \mathbf{M}_u, \mathbf{M}_\beta\}, \in \mathbb{R}^{n_\theta} \quad (40)$$

375 Particularly, the matrices  $\mathbf{P}, \Lambda, \mathbf{Q}, \mathbf{R}$  are constants that need to be identified from data, and  
376 account for the effects of coarse-graining on the stiffness and forcing matrices. The matrices  
377  $\mathbf{D}(\bar{\mathbf{u}}), \mathbf{E}(\bar{\mathbf{u}}), \mathbf{G}(\bar{\mathbf{u}})$  are state-dependent matrices, and account for the effects of coarse-graining  
378 on the advection matrix due to mesh motion. Leveraging the DG-FEM formula for the

<sup>379</sup> advection matrix in eq. (55c) in the Appendix, and noting that the ablating velocity in  
<sup>380</sup> eq. (4) imposes the boundary condition for the mesh motion, the state-dependent matrices  
<sup>381</sup> for the  $i$ -th component are written as,

$$\mathbf{D}(\bar{\mathbf{u}}) \approx \dot{\mathbf{w}}(\bar{\mathbf{u}}) \odot_r \mathbf{D}, \quad \mathbf{G}(\bar{\mathbf{u}}) \approx \mathbf{G} \odot_r \dot{\mathbf{w}}(\bar{\mathbf{u}}), \quad \mathbf{E}(\bar{\mathbf{u}}) \approx \dot{\mathbf{W}}(\bar{\mathbf{u}}) \odot \mathbf{E} \quad (41)$$

<sup>382</sup> where  $\dot{\mathbf{w}}(\bar{\mathbf{u}})$  is the SRM based on the observable temperature  $\bar{\mathbf{u}}$ ,  $\odot_r$  is the row-wise multiplication,  
<sup>383</sup> and  $\dot{\mathbf{W}}$  is the concatenation of  $\dot{\mathbf{w}}$  for  $\tilde{m}$  times, where  $\tilde{m}$  corresponds to the number  
<sup>384</sup> of hidden states per component, i.e.,  $m = N\tilde{m}$ .

<sup>385</sup> The PIROM in eq. (38) incorporates explicit information on the material properties,  
<sup>386</sup> boundary conditions, and surface recession, and is designed to generalize across parametric  
<sup>387</sup> variations in these inputs. Moreover, the hidden dynamics in eq. (34) are interpretable, as  
<sup>388</sup> these retain the functional form of the DG-FEM in eq. (8). The next step is focused on  
<sup>389</sup> identifying the unknown data-driven parameters  $\Theta$  characterizing the hidden dynamics.

### <sup>390</sup> 3.3 Learning the Hidden Dynamics

<sup>391</sup> Learning of the PIROM is achieved through a gradient-based neural-ODE-like approach [3].  
<sup>392</sup> For ease of presentation, consider the compact form of the PIROM in eq. (38),

$$\mathcal{D}(\dot{\mathbf{y}}, \mathbf{y}, \boldsymbol{\xi}, \mathcal{F}; \Theta) = \mathbf{0} \quad (42)$$

<sup>393</sup> where  $\boldsymbol{\xi}$  defines the model parameters, i.e., material properties and B' tables, while  $\mathcal{F}$   
<sup>394</sup> represents the forcing terms, i.e., the boundary conditions.

<sup>395</sup> Consider a dataset of  $N_s$  high-fidelity *surface temperature* observable trajectories  $\mathbf{z}_{\text{HF}}$ ,  
<sup>396</sup> sampled at  $p$  time instances  $\{t_k\}_{k=0}^{p-1}$ , for different parameter settings  $\{\boldsymbol{\xi}^{(l)}\}_{l=1}^{N_s}$  and forcing  
<sup>397</sup> functions  $\{\mathcal{F}^{(l)}(t)\}_{l=1}^{N_s}$ . The dataset is expressed as,

$$\mathcal{D} = \left\{ \left( t_k, \mathbf{z}_{\text{HF}}^{(l)}(t_k), \boldsymbol{\xi}^{(l)}, \mathcal{F}^{(l)}(t_k) \right) \right\}_{l=1}^{N_s}, \quad k = 0, 1, \dots, p-1 \quad (43)$$

<sup>398</sup> In this work, the dataset contains only surface temperature observables – all high-fidelity  
<sup>399</sup> information regarding the surface displacements *are assumed to be unavailable during learning*.  
<sup>400</sup>

<sup>401</sup> The learning problem is formulated as the following differentially-constrained problem,

$$\min_{\Theta} \quad \mathcal{J}(\Theta; \mathcal{D}) = \sum_{l=1}^{N_s} \int_{t_0}^{t_f} \ell \left( \mathbf{z}_u^{(l)}, \mathbf{z}_{\text{HF}}^{(l)} \right) dt \quad (44a)$$

$$\text{s.t.} \quad \mathbf{0} = \mathcal{D} \left( \dot{\mathbf{y}}^{(l)}, \mathbf{y}^{(l)}, \boldsymbol{\xi}^{(l)}, \mathcal{F}^{(l)}; \Theta \right) \quad (44b)$$

<sup>402</sup> for  $l = 1, 2, \dots, N_s$ , the objective is to minimize the discrepancy between the high-fidelity  
<sup>403</sup> and PIROM predictions for the  $l$ -th trajectory with  $\ell \left( \mathbf{z}_u^{(l)}, \mathbf{z}_{\text{HF}}^{(l)} \right) = \left\| \mathbf{z}_u^{(l)} - \mathbf{z}_{\text{HF}}^{(l)} \right\|_2^2$ .

<sup>404</sup> The gradient-based optimization loop is based on the adjoint variable  $\boldsymbol{\lambda}$ , governed by the

405 adjoint differential equation,

$$\frac{\partial \ell}{\partial \mathbf{y}} + \boldsymbol{\lambda}^\top \frac{\partial \mathcal{D}}{\partial \mathbf{y}} - \frac{d}{dt} \left( \boldsymbol{\lambda}^\top \frac{\partial \mathcal{D}}{\partial \dot{\mathbf{y}}} \right) = \mathbf{0} \quad (45a)$$

$$\boldsymbol{\lambda}(t_f)^\top \frac{\partial \mathcal{D}}{\partial \dot{\mathbf{y}}(t_f)} = \mathbf{0} \quad (45b)$$

406 Once  $\boldsymbol{\lambda}$  is solved, the gradient is computed as,

$$\nabla_{\Theta} \mathcal{J} = \frac{1}{N_s} \sum_{l=1}^{N_s} \int_{t_0}^{t_f} \left( \frac{\partial \ell}{\partial \Theta} + (\boldsymbol{\lambda}^{(l)})^\top \frac{\partial \mathcal{D}}{\partial \Theta} \right) dt \quad (46)$$

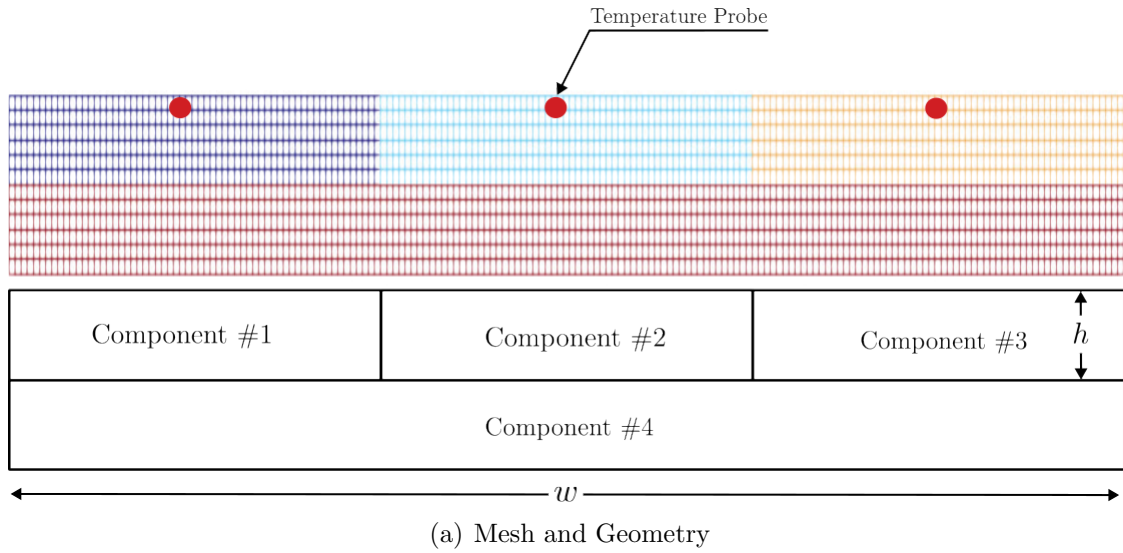
## 407 4 Application to Thermal Protection Systems

408 In this section, the proposed PIROM approach is applied to the analysis of thermo-ablative  
 409 multi-layered hypersonic TPS. The performance of the PIROM is evaluated in terms of the  
 410 three corners of the ITM in Fig. 1, across a wide range of boundary condition and SRM  
 411 model parametrizations for the TPS. The results show PIROM to be a promising candidate  
 412 for the solution of the impossible trinity of modeling, achieving RPM-level computational  
 413 efficiency and generalizability, while attaining high-fidelity model accuracy.

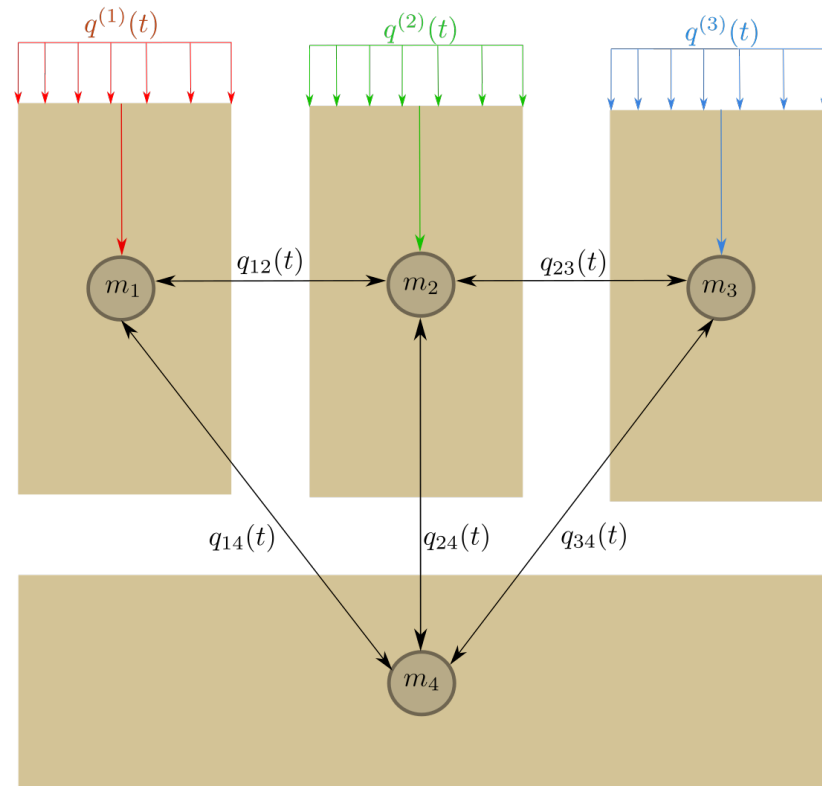
### 414 4.1 Problem Definition

415 Consider the two-dimensional TPS configuration shown in Fig. 3 with constant material  
 416 properties within each layer, dimensions, and BCs listed in Table 1. Such configuration is  
 417 representative of the TPS used for the initial concept 3.X vehicle in past studies [10], and in-  
 418 volves two main layers: an outer ablative layer, and an inner substrate layer. The top ablative  
 419 layer may be composed of different materials, such as PICA or Avcoat, while the substrate  
 420 layer is typically made of a high-temperature resistant material, such as carbon-carbon com-  
 421 posite [7]. The ablative layer, composed of  $\tilde{N} = 3$  ablative components, is subjected to  
 422 strong time-varying and non-uniform heating, while the substrate layer, composed of one  
 423 non-ablative component, is insulated adiabatically at the outer surface; the total number of  
 424 components is thus  $N = 4$ .

425 The lumped-mass representation of the TPS configuration is shown in Fig. 3(b), where  
 426 each component  $\Omega_i$  is represented by a lumped mass with uniform temperature  $u_i(t)$ . Details  
 427 regarding the derivation of the LCM for this configuration are provided in Appendix A.  
 428 The sources of non-linearities studied in this problem originate from the coupling between  
 429 the thermodynamics and temperature-dependent mesh motion, i.e., geometry-dependent  
 430 matrices, as well as the heterogeneities across material layers. As shown in Fig. 3, perfect  
 431 thermocouple devices are placed at the surfaces of the ablative layers for the collection of  
 432 the high-fidelity temperature signals that are used in the following sections for training and  
 433 testing the PIROM.



(a) Mesh and Geometry



(b) Lumped Mass Representation

Figure 3: Four-component TPS geometry and lumped-mass representation for the TPS.

Component	$w$ (cm)	$h$ (cm)	$\rho$ (kg/m <sup>3</sup> )	$c_p$ (J/kg·K)	$k$ (W/m·K)	$\alpha \times 10^{-6}$ (m/s·K)
#1	0.3	0.03	160	1200	0.2	1
#2	0.3	0.03	1800	900	5	1
#3	0.3	0.03	300	1500	0.15	1
#4	0.9	0.03	1600	800	10	0

Table 1: Description of TPS components, including thickness  $h$ , density  $\rho$ , specific heat capacity  $c_p$ , thermal conductivity  $k$ , and SRM parameter  $\alpha$ .

## 4.2 Problem Parametrization

The operating conditions of the TPS are specified by the boundary conditions, i.e., the heat flux, and the surface recession model (SRM). Specifically, the heat flux on the Neumann BC is parametrized using  $\boldsymbol{\xi}_{\text{BC}} = \{\xi_0, \xi_1, \xi_2\}$ , while the SRM is parametrized using  $\boldsymbol{\xi}_{\text{SRM}} = \{\alpha_1, \alpha_2, \alpha_3\}$ . Thus, the heat flux and SRM over the  $i$ -th ablative component are expressed as,

$$q_i(x, t; \boldsymbol{\xi}_{\text{BC}}) = \xi_0 e^{\xi_1 x} e^{\xi_2 t}, \quad \forall x \in \Gamma_{i,q}, \quad \dot{w}_i(z_{u,i}; \boldsymbol{\xi}_{\text{SRM}}) = \alpha_i (z_{u,i} - u_{0,i}), \quad i = 1, \dots, \tilde{N} \quad (47)$$

where  $\Gamma_{i,q}$ ,  $z_{u,i}$ , and  $u_{0,i}$  correspond to the Neumann BC surface, the PIROM's surface temperature prediction, and the initial temperature of the  $i$ -th ablative component, respectively. The parameters  $\xi_0$ ,  $\xi_1$ , and  $\xi_2$  control the heat flux magnitude, spatial variation, and temporal variation, respectively. The constant  $\alpha_i$  is a small material-dependent constant determined from the B' table [12], specifying the surface recession velocity for a given temperature.

## 4.3 Data Generation

Full-order solutions of the TPS are computed using the FEM multi-mechanics module of the **Aria** package [4], where the mesh is shown in Fig. 3. The mesh consists of 2196 total elements, with 366 elements for each ablative component and 1098 elements for the substrate component. All solutions are computed for one minute from an uniform initial temperature of  $T(x, t_0) = 300$  K. Given an operating condition  $\boldsymbol{\xi} = [\boldsymbol{\xi}_{\text{BC}}, \boldsymbol{\xi}_{\text{SRM}}]^\top$ , a full-order solution consists of then collection of time-varying temperature and displacement fields  $\left\{ \left( t_k, \mathbf{u}_{\text{HF}}^{(l)}(t_k), \mathbf{w}_{\text{HF}}^{(l)}(t_k), \boldsymbol{\xi}^{(l)} \right) \right\}_{k=0}^{p-1}$ , where  $p$  is the number of time steps with a step size of  $\Delta t \approx 10^{-3}$ . The observable trajectories are representative of near-wall thermocouple sensing of hypersonic flows involving heat transfer. At each time instance  $t_k$ , a temperature reading is recorded from each ablative component using the thermocouples shown in Fig. 3, resulting in three temperature signals, i.e., the observables  $\mathbf{z}_{textHF} \in \mathbb{R}^3$ . Therefore, each full-order solution produces one trajectory of observables  $\left\{ \left( t_k, \mathbf{z}_{\text{HF}}^{(l)}(t_k), \boldsymbol{\xi}^{(l)} \right) \right\}_{k=0}^{p-1}$ . The goal of the PIROM is to predict the surface temperature and displacement as accurately as possible.

460 **4.3.1 Definition of Training and Testing Datasets**

461 The range of parameters used to generate the training  $\mathcal{D}_1$  and testing  $\{\mathcal{D}_2, \mathcal{D}_3\}$  datasets  
 462 are listed in Table 1. The training and testing datasets are designed, respectively, to: (1)  
 463 minimize the information that the PIROM can “see”, and (2) to maximize the variabil-  
 464 ity of test operating conditions to examine the PIROM’s generalization performance. A  
 465 total of 110 normally-distributed data points for the BC parametrization are visualized in  
 466 Fig. 4(a), and the corresponding observable trajectories are shown in Figs. 4(b) and 4(c).  
 467 The training dataset  $\mathcal{D}_1$  includes 10 trajectories with randomly selected BC parameters from  
 468 the 110 points, with nominal SRM parameters  $\xi_{\text{SRM}} = \{1, 1, 1\} \times 10^{-6}$ . Note that although  
 469 Fig. 4(c) shows the surface displacements for all ablative components in  $\mathcal{D}_1$ , only the *surface*  
 470 *temperature is used for training the PIROM.*

471 Two additional datasets are generated for testing. The dataset  $\mathcal{D}_2$  includes the remaining  
 472 100 BC parameter values not considered in  $\mathcal{D}_1$ , and the high-fidelity simulation are generated  
 473 with the same nominal SRM parameters. The cases in the  $\mathcal{D}_3$  fixes the boundary condition  
 474 as shown in Fig. 4(a) and varies the SRM parameters as shown in Table. 1. The testing  
 475 datasets  $\mathcal{D}_2$  and  $\mathcal{D}_3$  are *out-of-distribution* (OOD) datasets, and are meant for testing the  
 476 generalizability of the ROMs to unseen BCs and SRMs, respectively.

477 **4.4 Performance Metrics**

478 The performance of the PIROM is evaluated by the metrics of prediction error and compu-  
 479 tational cost.

480 **Prediction Error** Consider one trajectory of high-fidelity surface temperature and dis-  
 481 placement data  $\left\{ \left( t_k, \mathbf{z}_{u,\text{HF}}^{(l)}(t_k), \mathbf{z}_{w,\text{HF}}^{(l)}(t_k) \right) \right\}_{k=0}^{p-1}$  for the  $l$ -th operating condition in the testing  
 482 datasets  $\mathcal{D}_2$  or  $\mathcal{D}_3$ . The difference  $e_i^{(l)}$  for the  $i$ -th predicted observable, denoted as  $z_i^{(l)}$ , is  
 483 computed as,

$$e_i^{(l)} = \frac{1}{\Delta z_i^{(l)}} \sqrt{\frac{1}{p} \sum_{k=0}^{p-1} \left( z_{i,\text{HF}}^{(l)}(t_k) - z_i^{(l)}(t_k) \right)^2} \quad (48)$$

484 for  $i = 1, 2, 3$  and  $z_i^{(l)} \in \{z_{i,u}^{(l)}, z_{i,w}^{(l)}\}$ , and where,

$$\Delta z_i^{(l)} = \max_{0 \leq k \leq p-1} z_{i,\text{HF}}^{(l)}(t_k) - \min_{0 \leq k \leq p-1} z_{i,\text{HF}}^{(l)}(t_k) \quad (49)$$

485 Subsequently, the prediction error of one trajectory is computed by a weighted sum based  
 486 on the area of each *ablative component*, resulting in the normalized root mean square error  
 487 (NRMSE) metric for one trajectory,

$$\text{NRMSE} = \frac{\sum_{i=1}^{\tilde{N}} |\Omega_i| e_i^{(l)}}{\sum_{i=1}^{\tilde{N}} |\Omega_i|} \times 100\% \quad (50)$$

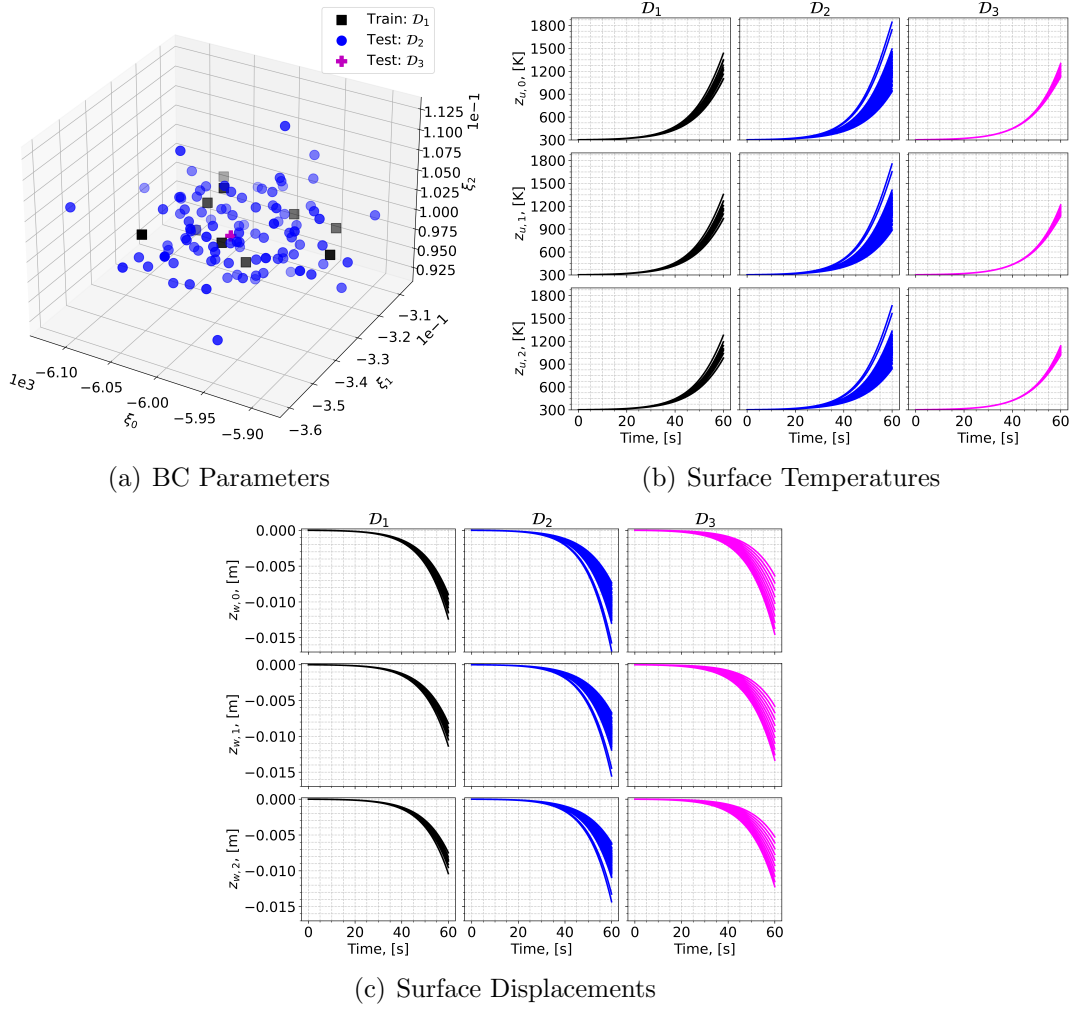


Figure 4: Boundary condition parameters, temperature observables, and displacement observables for the training and testing datasets. The variables  $z_{u,i}$  and  $z_{w,i}$  correspond to the surface temperature and displacement of the  $i$ -th ablative component, respectively.

488 For one dataset, the NRMSE is defined to be the average of the NRMSEs of all trajectories  
489 in the dataset.

490 **Computational Acceleration** The *computational acceleration* metric focuses on the quantification of the speedup factor  $\frac{\mathcal{T}_{\text{HF}}(\mathcal{D})}{\mathcal{T}_{\mathcal{M}}(\mathcal{D})}$ , where  $\mathcal{T}_{\text{HF}}(\mathcal{D})$  and  $\mathcal{T}_{\mathcal{M}}(\mathcal{D})$  correspond to the wall-clock time required by the high-fidelity model and the reduced-order model  $\mathcal{M}$  (i.e., PIROM or RPM) to evaluate all trajectories in the dataset  $\mathcal{D}$ , respectively. For a benchmark analysis of the computational costs during the training phase, please refer to Ref. [17].

## 495 4.5 Generalization to Boundary Conditions

496 To assess generalization to BC, the PIROM and RPM are evaluated on the  $\mathcal{D}_2$  dataset. Temperature trajectory predictions for a representative test case are shown in Figs. 5(a) and 5(b),  
497 where the PIROM accurately captures the surface temperature and displacement dynamics,  
498 while the RPM exhibits larger deviations and under-predicts surface displacements due to  
500 the averaging effects of the LCM. The mean NRMSE across all test cases in  $\mathcal{D}_2$  is shown  
501 in Figs. 5(e) and 5(f), where the PIROM consistently achieves errors of  $\approx 0.5\%$  for both  
502 temperature and displacement predictions, improving the RPM's accuracy by an order of  
503 magnitude. Figure 5 reports the average substrate temperature, where the LCM remains  
504 highly accurate due to the symmetric TPS geometry, adiabatic BCs, and negligible thermal  
505 gradients within the substrate. Although the PIROM is trained only on the surface temperatures  
506 of the three ablative components, its hidden dynamics retain the LCM's accuracy  
507 for this untrained observable, demonstrating the PIROM's ability to generalize and preserve  
508 the underlying physics of the reduced-physics backbone.

## 509 4.6 Generalization to Surface Recession Models

510 The generalization performance of the PIROM and RPM is also evaluated on surface recession models using the  $\mathcal{D}_3$  dataset. As detailed in Table 1, the SRM parameter  $\alpha$  in  $\mathcal{D}_3$  is perturbed 10 times by up to  $\pm 50\%$  from their nominal values. The SRM model perturbation  
511 introduces significant changes to the ablative layer dynamics, potentially increasing the rate  
512 of ablation at lower temperatures, as shown in Figs. 5(c) and 5(d). The PIROM, without  
513 considering any SRM variations during training, is able to accurately predict the surface tem-  
514 perature and displacement dynamics for the perturbed SRMs. Figures 5(e) and 5(f) show  
515 the mean NRMSE across all test cases in  $\mathcal{D}_3$ , where the PIROM consistently achieves errors  
516 below 1.5% for both temperature and displacement predictions, and consistently improves  
517 the RPM's accuracy by approximately an order of magnitude.  
518

## 520 4.7 Computational Cost

521 All computations are performed in serial for fairness on an Intel Xeon (R) Gold 6258R  
522 CPU 2.70GHz computer with 62 GB of RAM. The numerical integration for the RPM  
523 and PIROM models are performed using SciPy's `solve_ivp` function with default settings.  
524 Provided a parametrization for the BC and SRM, the high-fidelity FEM simulation takes  
525 about  $\approx 60$  seconds, the RPM takes about  $\approx 0.137$  seconds, and the PIROM takes about

526  $\approx 0.280$  seconds. Therefore, during evaluation both the RPM and PIROM achieve speedup  
527 factors of approximately 438 and 214, respectively, over the high-fidelity model. As a result,  
528 the PIROM and RPM are *two-orders-of-magnitude faster* than the high-fidelity model. The  
529 PIROM nearly preserves the computational efficiency of the RPM (about twice as expensive  
530 as the RPM), while achieving significantly higher accuracy and generalization capabilities.  
531 The results demonstrate the benefits of physics-infused modeling for the development of  
532 efficient and generalizable ROMs for complex multi-physics systems.

## 533 4.8 Summary of Results

534 The results presented in this section demonstrate the accuracy, generalizability, and com-  
535 putational efficiency of the proposed PIROM approach for the analysis of thermo-ablative  
536 multi-layered hypersonic TPS. The PIROM consistently achieves low prediction errors below  
537 1% for both surface temperature and displacement across a range of unseen boundary con-  
538 ditions and surface recession models. Furthermore, the PIROM retains the computational  
539 efficiency of traditional RPMs, achieving speedup factors of over 200 times compared to high-  
540 fidelity FEM simulations. The generalization capabilities of the PIROM are attributed to its  
541 hybrid structure: a physics-based LCM backbone that ensures consistency with the under-  
542 lying thermodynamics, while a data-driven correction mechanism captures the un-resolved  
543 dynamics.

## 544 5 Conclusions

545 This work presents the development and validation of the *scientific machine learning* frame-  
546 work termed *Physics-Informed Reduced Order Model* (PIROM) for simulating the transient  
547 thermo-ablative response of hypersonic thermal protection systems (TPS) subjected to hy-  
548 personic aerodynamic heating. Using coarse-graining on a DG-FEM model and the Mori-  
549 Zwanzig formalism, the PIROM formulation in Ref. [17] is extended to account for non-  
550 decomposing ablative material response. The PIROM builds upon the following two key  
551 components: (1) a first-order physics-based model, i.e., the LCM and SRM, for low-fidelity  
552 predictions of the transient thermo-ablative TPS response; and (2) a data-driven closure to  
553 the non-Markovian term in the generalized Langevin equation (GLE). The non-Markovian  
554 closure is recast as a set of hidden states that evolve according to a data-driven dynamical  
555 system that is learned from a sparse collection of high-fidelity temperature signals.

556 The results demonstrate that the PIROM framework effectively reconciles the trade-  
557 offs between accuracy, generalizability, and efficiency of the ITM for simulating ablating  
558 hypersonic TPS. The PIROM consistently achieves mean observable prediction errors of  
559  $\approx 0.5\%$  for a wide range of extrapolative settings of model parameters, involving time-and-  
560 space varying boundary conditions and SRM models. Notably, the PIROM improves the  
561 RPM's accuracy by an order of magnitude while preserving its computational efficiency,  
562 physical interpretability, and parametric generalizability. Moreover, the PIROM delivers  
563 online evaluations that are two orders of magnitude faster than the FOM. These results  
564 highlight the PIROM's potential as a promising framework for optimizing multi-physical  
565 dynamical systems, such as TPS under diverse operating conditions.

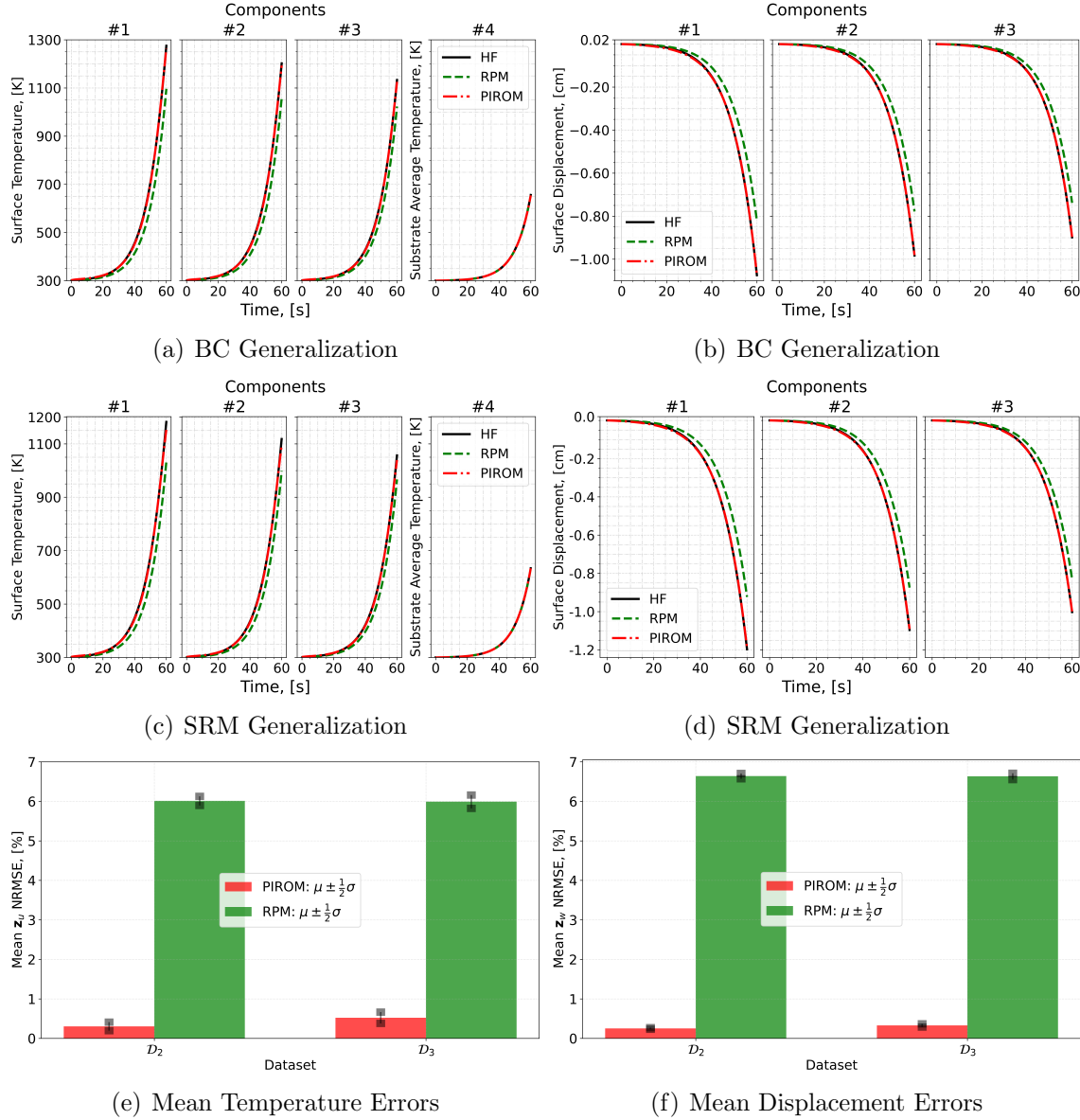


Figure 5: PIROM predictions against high-fidelity solutions for (a)-(b) BC generalization, (c)-(d) SRM generalization, and (e)-(f) mean errors across testing datasets.

## 566 A Technical Details

567 This appendix presents the technical details of the PIROM framework applied to the trans-  
 568ient modeling of thermo-ablative TPS. The first section provides the mathematical details  
 569 for the definition of the DG-FEM. The second section details the coarse-graining proce-  
 570 dures performed on the DG-FEM representation of the TPS. The third section presents the  
 571 derivation of the LCM model from an energy-conservation perspective.

### 572 A.1 Full-Order Model

573 To obtain the full-order numerical solution, the governing equation is spatially discretized  
 574 using variational principles of Discontinuous Galerkin (DG) to result in a high-dimensional  
 575 system of ordinary differential equations (ODEs). The DG-FEM model is written in an  
 576 element-wise form, which is beneficial for subsequent derivations of the lower-order models.  
 577 Note that the choice of DG approach here is mainly for theoretical convenience in the sub-  
 578 sequent coarse-graining formulation. In the numerical results, the full-order TPS ablation  
 579 simulations is computed using standard FEM instead, and the equivalence between DG and  
 580 standard FEM is noted upon their convergence.

#### 581 A.1.1 Domain Discretization

582 Consider a conforming mesh partition of the domain, as shown in Fig. DOMAIN, where each  
 583 element belongs to one and only one component. Denote the collection of all  $M$  elements  
 584 as  $\{E_i\}_{i=1}^M$ . To ease the description of the DG model, a graph structure is employed. The  
 585 elements are treated as vertices, the set of which is denoted  $\mathcal{V} = \{m\}_{m=1}^M$ . Two neighboring  
 586 elements,  $E_i$  and  $E_j$ , are connected by an edge  $(i, j)$ , and the shared boundary between them  
 587 is denoted  $e_{ij}$ . The collection of all edges are denoted  $\mathcal{E}$ , and  $\mathcal{G}$  is referred to as a graph.  
 588 In the graph, the edges are unidirected, meaning if  $(i, j) \in \mathcal{E}$  then  $(j, i) \in \mathcal{E}$ . Furthermore,  
 589 denote the neighbors of the  $i$ -th element as  $\mathcal{N}_i = \{j | (i, j) \in \mathcal{E}\}$ . Lastly, for the ease of  
 590 notation, introduce two special indices:  $T$  for the boundary of an element that overlaps with  
 591 the Dirichlet boundary condition, and similarly  $q$  for the Neumann boundary condition.

#### 592 A.1.2 Weak Form of Discontinuous Galerkin Method

593 Choosing appropriate basis functions  $\phi_k$  and  $\phi_l$  and using the Interior Penalty Galerkin  
 594 (IPG) scheme [5], the variational bilinear form for eq. (1a) is,

$$\sum_{i=1}^M a_{\epsilon,i}(\phi_k, \phi_l) = \sum_{i=1}^M L_i(\phi_k) \quad (51)$$

595 where  $\epsilon$  is an user-specified parameter and,

$$a_{\epsilon,i}(\phi_k, \phi_l) = \int_{E^{(i)}} \left( \rho c_p \phi_k \frac{\partial \phi_l}{\partial t} + \nabla \phi_k \cdot (\mathbf{k} \nabla \phi_l) - \rho c_p \phi_k \mathbf{v} \cdot \nabla \phi_l \right) dE^{(i)} \quad (52a)$$

$$\begin{aligned} &= - \sum_{j \in \mathcal{N}_i \cup \{T_b\}} \int_{e_{ij}} \{ \mathbf{k} \nabla \phi_k \cdot n \} [\phi_l] de_{ij} + \epsilon \sum_{j \in \mathcal{N}_i \cup \{T_b\}} \int_{e_{ij}} \{ \mathbf{k} \nabla \phi_l \cdot n \} [\phi_k] de_{ij} \\ &\quad + \sigma \sum_{j \in \mathcal{N}_i \cup \{T_b\}} \int_{e_{ij}} [\phi_k] [\phi_l] de_{ij} \end{aligned} \quad (52b)$$

$$L_i(v) = \epsilon \sum_{j \in \mathcal{N}_i \cup \{T_b\}} \int_{e_{ij}} (\mathbf{k} \nabla \phi_l \cdot n) T_b de_{ij} + \int_{e_{iq}} \phi_k q_b de_{iq} + \sigma \int_{e_{iT}} \phi_k T_b de_{iT} \quad (52c)$$

596 In the bi-linear form above, the notations  $[]$  and  $\{ \}$  are respectively the jumps and averages  
597 at the boundary  $e_{ij}$  share by two elements  $E_i$  and  $E_j$ ,

$$[u] = u|_{E_i} - u|_{E_j}, \quad \{u\} = \frac{1}{2} \left( u|_{E_i} + u|_{E_j} \right), \quad \text{for } x \in e_{ij} = E_i \cap E_j$$

598 Furthermore, in the bi-linear form, the terms associated with  $\sigma$  are introduced to enforce  
599 the Dirichlet boundary conditions;  $\sigma$  is a penalty factor whose value can depend on the size  
600 of an element. Depending on the choice of  $\epsilon$ , the bi-linear form corresponds to symmetric  
601 IPG ( $\epsilon = -1$ ), non-symmetric IPG ( $\epsilon = 1$ ), and incomplete IPG ( $\epsilon = 0$ ). All these schemes  
602 are consistent with the original PDE and have similar convergence rate with respect to mesh  
603 size. In the following derivations, the case  $\epsilon = 0$  is chosen for the sake of simplicity.

#### 604 A.1.3 Discontinuous Galerkin Model

605 Next, the DG-based model is written in an element-wise form. For the  $i$ -th element, use a  
606 set of  $P$  trial functions to represent the temperature as in eq. (6). Without loss of generality,  
607 the trial functions are assumed to be orthogonal, so that  $\int_{E^{(i)}} \phi_k^{(i)}(x) \phi_l^{(i)}(x) dx = |E^{(i)}| \delta_{kl}$ ,  
608 where  $|E^{(i)}|$  is the area ( $n_d = 2$ ) or volume ( $n_d = 3$ ) of the  $i$ -th element, and  $\delta_{kl}$  is the  
609 Kronecker delta.

610 Using test functions same as trial functions, the dynamics  $\mathbf{u}^{(i)}$  is obtained by evaluating  
611 the element-wise bi-linear forms,

$$a_{\epsilon,i}(\phi_k^{(i)}, T^{(i)}) = L_i(\phi_k^{(i)}), \quad k = 1, 2, \dots, P \quad (53)$$

612 The above procedure yields,

$$\mathbf{A}^{(i)} \dot{\mathbf{u}}^{(i)} = (\mathbf{B}^{(i)} + \mathbf{C}^{(i)}(t)) \mathbf{u}^{(i)} + \sum_{j \in \mathcal{N}_i \cup \{T_b\}} \left( \mathbf{B}_{ij}^{(i)} \mathbf{u}^{(i)} + \mathbf{B}_{ij}^{(j)} \mathbf{u}^{(j)} \right) + \mathbf{f}^{(i)}(t) \quad (54)$$

613 where for  $k, l = 1, 2, \dots, P$ ,

$$[\mathbf{A}^{(i)}]_{kl} = \int_{E^{(i)}} \rho c_p \phi_k^{(i)} \phi_l^{(i)} dE^{(i)} \quad (55a)$$

$$[\mathbf{B}^{(i)}]_{kl} = - \int_{E^{(i)}} (\nabla \phi_k^{(i)}) \cdot (\mathbf{k} \nabla \phi_l^{(i)}) dE^{(i)} \quad (55b)$$

$$[\mathbf{C}^{(i)}]_{kl} = \int_{E^{(i)}} \rho c_p \phi_k^{(i)} \mathbf{v}^{(i)} \cdot \nabla \phi_l^{(i)} dE^{(i)} \quad (55c)$$

$$[\mathbf{B}_{ij}^{(i)}] = \int_{e_{ij}} \left\{ \mathbf{k} \nabla \phi_k^{(i)} \cdot \hat{n} \right\} \phi_l^{(i)} - \sigma [\phi_k^{(i)}] \phi_l^{(i)} de_{ij} \quad (55d)$$

$$[\mathbf{B}_{ij}^{(j)}] = \int_{e_{ij}} - \left\{ \mathbf{k} \nabla \phi_k^{(i)} \cdot \hat{n} \right\} \phi_l^{(j)} + \sigma [\phi_k^{(i)}] \phi_l^{(j)} de_{ij} \quad (55e)$$

$$[\mathbf{f}^{(i)}]_k = \int_{e_{iq}} \phi_k^{(i)} q_b de_{iq} + \sigma \int_{e_{iT}} \phi_k^{(i)} de_{iT} \quad (55f)$$

614 The matrices  $\mathbf{A}^{(i)} \in \mathbb{R}^{P \times P}$ ,  $\mathbf{B}^{(i)} \in \mathbb{R}^{P \times P}$ , and  $\mathbf{C}^{(i)} \in \mathbb{R}^{P \times P}$  are respectively the capacitance,  
615 conductivity, and advection matrices for element  $i$ . These matrices depend on  $\rho$ ,  $c_p$ ,  $\mathbf{k}$ , and  
616  $\mathbf{v}$ , and hence can be non-linear functions of  $\mathbf{u}^{(i)}$ . Since the trial functions are orthogonal, if  
617  $\rho c_p$  is constant within an element,  $\mathbf{A}^{(i)}$  is diagonal; otherwise,  $\mathbf{A}_i$  is symmetric and positive  
618 definite as  $\rho c_p > 0$ .

619 For compactness, the element-wise model in eq. (54) is also written in matrix form,

$$\mathbf{A}(\dot{\mathbf{u}}) = [\mathbf{B}(\mathbf{u}) + \mathbf{C}(\mathbf{u})] \mathbf{u} + \mathbf{f}(t) \quad (56)$$

620 where  $\mathbf{u} = [\mathbf{u}^{(1)}, \mathbf{u}^{(2)}, \dots, \mathbf{u}^{(M)}]^T \in \mathbb{R}^{MP}$  includes all DG variables,  $\mathbf{f} = [\mathbf{f}^{(1)}, \mathbf{f}^{(2)}, \dots, \mathbf{f}^{(M)}]^T \in$   
621  $\mathbb{R}^{MP}$ ,  $\mathbf{A}$  and  $\mathbf{C}$  are matrices of  $M$  diagonal blocks whose  $i$ -th blocks are  $\mathbf{A}^{(i)}$  and  $\mathbf{C}^{(i)}$ , and  
622  $\mathbf{B}$  is a matrix of  $M \times M$  blocks whose  $(i, j)$ -th block is,

$$\mathbf{B}_{ij} = \begin{cases} \mathbf{B}^{(i)} + \sum_{j \in \mathcal{N}_i \cup \{T_b\}} \mathbf{B}_{ij}^{(i)}, & i = j \\ \mathbf{B}_{ij}^{(j)}, & i \neq j \end{cases} \quad (57)$$

623 The dependency of  $\mathbf{A}$ ,  $\mathbf{B}$ , and  $\mathbf{C}$  on  $\mathbf{u}$  is explicitly noted in eq. (56), which is the source of  
624 non-linearity in the current TPS problem. Moreover, the mesh velocity  $\mathbf{v}$  varies with space  
625 and time, and thus the advection matrix  $\mathbf{C}$  varies with time as a function of  $q_b$ .

## 626 A.2 Coarse-Graining of Dynamics

627 The LCM is obtained by coarse-graining the full-order DG-FEM. This coarse-graining proce-  
628 dure produces resolved  $\mathbf{r}^{(1)}(\mathbf{u}, t)$  and residual  $\mathbf{r}^{(2)}(\mathbf{u}, t)$  dynamics as in eq. (23). This section  
629 presents the detail derivations and magnitude analysis for the resolved and residual dynam-  
630 ics.

631 **A.2.1 Resolved Dynamics**

632 Using eq. (20), the resolved dynamics is computed as follows,

$$\mathbf{r}^{(1)}(\mathbf{u}, t) = \mathcal{P} [\Phi^+ \mathbf{A}(\mathbf{u})^{-1} (\mathbf{B}(\mathbf{u})\mathbf{u} + \mathbf{C}(\mathbf{u})\mathbf{u} + \mathbf{f}(t))] \quad (58a)$$

$$= \Phi^+ \mathbf{A}(\mathbf{P}\mathbf{u})^{-1} \mathbf{P}\mathbf{B}(\mathbf{P}\mathbf{u}) \mathbf{P}\mathbf{u} + \Phi^+ \mathbf{A}(\mathbf{P}\mathbf{u})^{-1} \mathbf{P}\mathbf{C}(\mathbf{P}\mathbf{u}) \mathbf{P}\mathbf{u} \\ + \Phi^+ \mathbf{A}(\mathbf{P}\mathbf{u})^{-1} \mathbf{P}\mathbf{f}(t, \mathbf{P}\mathbf{u}) \quad (58b)$$

$$= \underbrace{\Phi^+ \mathbf{A}(\Phi\bar{\mathbf{u}})^{-1} \Phi}_{\#1} \underbrace{\Phi^+ \mathbf{B}(\Phi\bar{\mathbf{u}}) \Phi\bar{\mathbf{u}}}_{\#2} + \Phi^+ \mathbf{A}(\Phi\bar{\mathbf{u}})^{-1} \Phi \underbrace{\Phi^+ \mathbf{C}(\Phi\bar{\mathbf{u}}) \Phi\bar{\mathbf{u}}}_{\#3} \\ + \Phi^+ \mathbf{A}(\Phi\bar{\mathbf{u}})^{-1} \Phi \underbrace{\Phi^+ \mathbf{f}(t, \Phi\bar{\mathbf{u}})}_{\#4} \quad (58c)$$

633 Detailed derivations for the #1, #2, and #4 terms can be found in Ref. [17]. The effects of  
634 coarse-graining on the advection term #3 are analyzed next.

635 **Term #3** The  $\mathbf{C}(\mathbf{u}) \in \mathbb{R}^{MP \times MP}$  matrix contains  $M$  diagonal of size  $P \times P$ , since the  
636 basis functions are defined locally on each element. Therefore,  $[\mathbf{C}(\mathbf{u})]_{ij} = \mathbf{0}$  for all  $i \neq j$  with  
637  $i, j = 1, 2, \dots, M$ . It follows that for  $k, l = 1, 2, \dots, N$ ,

$$[\Phi^+ \mathbf{C}(t, \Phi\bar{\mathbf{u}}) \Phi]_{kl} = \sum_{i=1}^M \sum_{j=1}^M \boldsymbol{\varphi}_i^{k+} [\mathbf{C}(t, \Phi\bar{\mathbf{u}})]_{ij} \boldsymbol{\varphi}_j^l \quad (59a)$$

$$= \sum_{i=1}^M \boldsymbol{\varphi}_i^{k+} [\mathbf{C}(t, \Phi\bar{\mathbf{u}})]_{ii} \boldsymbol{\varphi}_i^l \quad (59b)$$

$$= \sum_{i \in \mathcal{V}_k} \boldsymbol{\varphi}_i^{k+} [\mathbf{C}(t, \Phi\bar{\mathbf{u}})]_{ii} \boldsymbol{\varphi}_i^l \quad (59c)$$

638 where in the second row, the fact that  $[\mathbf{C}(\mathbf{u})]_{ij} = 0$  for all  $i \neq j$  is used, and in the last row,  
639 the fact that  $\boldsymbol{\varphi}_i^{k+} = 0$  for all  $i \notin \mathcal{V}_k$  is used. Now, considering that  $[\mathbf{C}(\mathbf{u})]_{ii}$  has a (1, 1)-th  
640 zero element, i.e.,  $[\mathbf{C}(t, \Phi\bar{\mathbf{u}})]_{ii} = 0$ , and that if  $k \neq l$  then  $i \notin \mathcal{V}_l$  and thus  $\boldsymbol{\varphi}_i^l = \mathbf{0}$ , it follows  
641 that for some index  $i \in \mathcal{V}_k$ ,

$$\boldsymbol{\varphi}_i^{k+} [\mathbf{C}(t, \Phi\bar{\mathbf{u}})]_{ii} \boldsymbol{\varphi}_i^l = \boldsymbol{\varphi}_i^{k+} [\mathbf{C}(t, \Phi\bar{\mathbf{u}})]_{ii} \boldsymbol{\varphi}_i^k = \frac{|E_i|}{|\Omega_k|} [C_{11}(t, \Phi\bar{\mathbf{u}})]_{ii} = 0 \quad (60)$$

642 The matrix  $[\Phi^+ \mathbf{C}(t, \Phi\bar{\mathbf{u}}) \Phi]_{kl} = 0$  for all  $k, l = 1, 2, \dots, N$ , and thus,

$$\bar{\mathbf{C}}(t, \bar{\mathbf{u}}) = \Phi^+ \mathbf{C}(t, \Phi\bar{\mathbf{u}}) \Phi = \mathbf{0} \quad (61)$$

643 as indicated by the LCM in eq. (9).

644 **A.2.2 Magnitude Analysis for Residual Dynamics**

645 Next, the magnitude of the residual dynamics  $\mathbf{r}^{(2)}(\mathbf{u}, t)$  is analyzed to pinpoint the missing  
646 physics in the LCM. By definition,

$$\mathbf{r}^{(2)}(\mathbf{u}, t) = \dot{\bar{\mathbf{u}}} - \mathbf{r}^{(1)}(\bar{\mathbf{u}}, t) \quad (62a)$$

$$= \Phi^+ \mathbf{r}(\mathbf{u}, t) - \mathbf{r}^{(1)}(\mathbf{u}, t) \quad (62b)$$

$$\begin{aligned} &= \underbrace{\Phi^+ \mathbf{A}(\mathbf{u})^{-1} \mathbf{B}(\mathbf{u}) \mathbf{u} - \bar{\mathbf{A}}(\bar{\mathbf{u}})^{-1} \bar{\mathbf{B}}(\bar{\mathbf{u}}) \bar{\mathbf{u}}}_{\#1} + \underbrace{\Phi^+ \mathbf{A}(\mathbf{u})^{-1} \mathbf{C}(\mathbf{u}) \mathbf{u} - \bar{\mathbf{A}}(\bar{\mathbf{u}})^{-1} \bar{\mathbf{C}}(\bar{\mathbf{u}}) \bar{\mathbf{u}}}_{\#2} \\ &\quad + \underbrace{\Phi^+ \mathbf{A}(\mathbf{u})^{-1} \mathbf{f}(t) - \bar{\mathbf{A}}(\bar{\mathbf{u}})^{-1} \bar{\mathbf{f}}(t)}_{\#3} \end{aligned} \quad (62c)$$

647 The magnitude analysis for terms  $\#1$  and  $\#3$  can be found in Ref. [17]. The analysis for  
648 term  $\#2$  is presented next. Let  $\mathbf{D}(\bar{\mathbf{u}}) = \mathbf{A}(\Phi \bar{\mathbf{u}})^{-1} \mathbf{P} \mathbf{C}(t, \Phi \bar{\mathbf{u}})$ , then,

$$\Phi^+ \mathbf{A}(\mathbf{u})^{-1} \mathbf{C}(\mathbf{u}) \mathbf{u} - \bar{\mathbf{A}}(\bar{\mathbf{u}})^{-1} \bar{\mathbf{C}}(\bar{\mathbf{u}}) \bar{\mathbf{u}} \quad (63a)$$

$$= \Phi^+ \mathbf{A}(\mathbf{u})^{-1} \mathbf{C}(\mathbf{u}) \mathbf{u} - \Phi^+ \mathbf{A}(\Phi \bar{\mathbf{u}})^{-1} \mathbf{P} \mathbf{C}(t, \Phi \bar{\mathbf{u}}) \Phi \Phi^+ \mathbf{u} \quad (63b)$$

$$= \Phi^+ \mathbf{A}^{-1}(\mathbf{u}) \mathbf{C}(\mathbf{u}) \mathbf{u} - \Phi^+ \mathbf{D}(\bar{\mathbf{u}}) \Phi \Phi^+ \mathbf{u} \quad (63c)$$

$$(63d)$$

649 where  $\mathbf{P} = \Phi \Phi^+$ . Thus,

$$\|\Phi^+ \mathbf{A}(\mathbf{u})^{-1} \mathbf{C}(\mathbf{u}) \mathbf{u} - \bar{\mathbf{A}}(\bar{\mathbf{u}})^{-1} \bar{\mathbf{C}}(\bar{\mathbf{u}}) \bar{\mathbf{u}}\| \quad (64a)$$

$$\leq \|\Phi^+ \mathbf{A}^{-1}(\mathbf{u}) \mathbf{C}(\mathbf{u}) \mathbf{u} - \Phi^+ \mathbf{D}(\bar{\mathbf{u}}) \mathbf{u}\| + \|\Phi^+ \mathbf{D}(\bar{\mathbf{u}}) \mathbf{u} - \Phi^+ \mathbf{D}(\bar{\mathbf{u}}) \Phi \Phi^+ \mathbf{u}\| \quad (64b)$$

$$\leq \|\Phi^+\| \underbrace{\|\mathbf{A}^{-1}(\mathbf{u}) \mathbf{C}(\mathbf{u}) \mathbf{u} - \mathbf{D}(\bar{\mathbf{u}}) \mathbf{u}\|}_{\#1} + \|\Phi^+ \mathbf{D}(\bar{\mathbf{u}})\| \underbrace{\|\mathbf{u} - \Phi \Phi^+ \mathbf{u}\|}_{\#2} \quad (64c)$$

650 where term  $\#2$  is due to the approximation of non-uniform temperature as constants, and  
651 term  $\#1$  is the error in the advection dynamics due to coarse-graining.

652 **A.3 Lumped Capacitance Model**

653 The following assumptions are employed: (1) the temperature in component  $(i)$  is described  
654 by a scalar time-varying average temperature  $\bar{u}^{(i)}$ , (2) between neighboring components  $(i)$   
655 and  $(j)$  the heat flux is approximated as,

$$q_{ij} = \frac{\bar{u}^{(j)} - \bar{u}^{(i)}}{R_{ij}} \quad (65)$$

656 where  $R_{ij}$  is the thermal resistance. Empirically, for a component of isotropic heat conduction  
657 with thermal conductivity  $k$ , length  $\ell$ , and cross-section area  $A$ , the thermal resistance is  $R = \ell/kA$ . Between  
658 components  $i$  and  $j$ , define  $R_{ij} = R_i + R_j$ . In addition, the heat flux due to Dirichlet  
659 boundary condition is computed as  $q_{iT} = (T_b - \bar{u}^{(i)})/R_i$ .

660 At component  $i$ , the dynamics of LCM are given by,

$$\int_{E^{(i)}} \rho c_p \dot{\bar{u}}^{(i)} dE^{(i)} = \left( \sum_{j \in \mathcal{N}_i} \int_{e_{ij}} \frac{\bar{u}^{(j)} - \bar{u}^{(i)}}{R_{ij}} de_{ij} \right) + \int_{e_{iq}} q_b de_{iq} + \int_{e_{iT}} \frac{T_b - \bar{u}^{(i)}}{R_i} de_{iT} \quad (66a)$$

$$\bar{A}^{(i)} \dot{\bar{u}}^{(i)} = \left( \sum_{j \in \mathcal{N}_i} \frac{|e_{ij}|}{R_{ij}} (\bar{u}^{(j)} - \bar{u}^{(i)}) \right) + |e_{iq}| \bar{q}^{(i)} + \frac{|e_{iT}|}{R_i} (\bar{T}^{(i)} - \bar{u}^{(i)}) \quad (66b)$$

$$= \sum_{j \in \mathcal{N}_i} \left( -\frac{|e_{ij}|}{R_{ij}} \bar{u}^{(i)} + \frac{|e_{ij}|}{R_{ij}} \bar{u}^{(j)} \right) + \left( -\frac{|e_{iT}|}{R_i} \bar{u}^{(i)} \right) + \left( |e_{iq}| \bar{q}^{(i)} + \frac{|e_{iT}|}{R_i} \bar{T}^{(i)} \right) \quad (66c)$$

$$= \sum_{j \in \mathcal{N}_i \cup \{T_b\}} \left( \bar{B}_{ij}^{(i)} \bar{u}^{(i)} + \bar{B}_{ij}^{(j)} \bar{u}^{(j)} \right) + \bar{f}^{(i)} \quad (66d)$$

661 where in eq. (66b)  $|e|$  denotes the length ( $d = 2$ ) or area ( $d = 3$ ) of a component boundary  
662  $e$ . The  $\bar{A}^{(i)}$ ,  $\bar{B}_{ij}^{(i)}$ , and  $\bar{B}_{ij}^{(j)}$  quantities are provided in eq. (12).

663 The lumped-mass representation for the four-component TPS is shown in Fig. ???. Let  
664  $v_i$  represent the area of the  $i$ -th element,  $\overline{\rho c_p}_i$ , the heat capacity evaluated using the average  
665 temperature  $\bar{u}^{(i)}$ , and  $1/R_{ij} = 1/R_i(\bar{u}^{(i)}) + 1/R_j(\bar{u}^{(j)})$  the equivalent thermal resistance  
666 between elements  $i$  and  $j$ . Leveraging the formulas from eqs. (11) and (12), the LCM  
667 matrices are given by,

$$\bar{\mathbf{A}} = \begin{bmatrix} \overline{\rho c_p}_1 v_1 & 0 & 0 & 0 \\ 0 & \overline{\rho c_p}_2 v_2 & 0 & 0 \\ 0 & 0 & \overline{\rho c_p}_3 v_3 & 0 \\ 0 & 0 & 0 & \overline{\rho c_p}_4 v_4 \end{bmatrix}, \quad (67a)$$

$$\bar{\mathbf{B}} = \begin{bmatrix} \frac{1}{R_{12}} + \frac{1}{R_{14}} & -\frac{1}{R_{12}} & 0 & -\frac{1}{R_{14}} \\ -\frac{1}{R_{12}} & \frac{1}{R_{12}} + \frac{1}{R_{24}} + \frac{1}{R_{23}} & -\frac{1}{R_{23}} & -\frac{1}{R_{24}} \\ 0 & -\frac{1}{R_{32}} & \frac{1}{R_{32}} + \frac{1}{R_{34}} & -\frac{1}{R_{34}} \\ -\frac{1}{R_{14}} & -\frac{1}{R_{24}} & -\frac{1}{R_{34}} & \frac{1}{R_{14}} + \frac{1}{R_{24}} + \frac{1}{R_{34}} \end{bmatrix}, \quad \bar{\mathbf{f}} = \begin{bmatrix} \bar{q}^{(1)} \\ \bar{q}^{(2)} \\ \bar{q}^{(3)} \\ 0 \end{bmatrix} \quad (67b)$$

## 668 References

- [1] Adam J. Amar, A. Brandon Oliver, Benjamin S. Kirk, Giovanni Salazar, and Justin Drob. Overview of the charring ablator response (char) code. In AIAA, editor, *AIAA Aviation Forum*, 2016.
- [2] Guy L. Bergel, Frank B. Beckwith, Gabel J. de Frias, Kevin M. Manktelow, Mark T. Merewether, Scott T. Miller, Krishen J. Parmar, Timothy S. Shelton, Jesse T. Thomas, Jeremy T. Trageser, Benjamin T. Treweek, Michael V. Veilleux, and Ellen B. Wagman. *Sierra/SolidMechanics 5.6 User's Manual*, 2022.
- [3] Ricky T. Q. Chen, Yulia Rubanova, Jesse Bettencourt, and David Duvenaud. Neural ordinary differential equations, 2019.

- [4] Jonathan Clausen, Victor Brunini, Lincoln Collins, Robert C Knaus, Alec Kucala, Stephen Lin, Daniel Robert Moser, Malachi Phillips, Thomas Michael Ransegrenola, Samuel Ramirez Subia, et al. Sierra multimechanics module: Aria verification manual-version 5.22. Technical report, Sandia National Lab.(SNL-NM), Albuquerque, NM (United States), 2024.
- [5] Gary Cohen and Sebastien Pernet. *Finite Element and Discontinuous Galerkin Methods for Transient Wave Equations*. Springer Dordrecht, Le Chesnay and Toulouse France, 2018.
- [6] Jianhao Fang, Weifei Hu, Zhenyu Liu, Yuhao Zhou, Chao Wei, and Jianrong Tan. A reduced order finite element-informed surrogate model for approximating global high-fidelity simulations. *Structural and Multidisciplinary Optimization*, 67(12), 2024.
- [7] Matthew Gasch, Keith Peterson, Mairead Stackpoole, Ethiraj Venkatapathy, Gregory Gonzales, and Kyle Hendrickson. Development of advanced ablative carbon phenolic tps for future nasa missions and commercial space. In *38th Annual Small Satellite Conference*, Logan, Utah, May 2024.
- [8] Micah A. Howard and Ben F. Blackwell. A multi-dimensional finite element based solver for decomposing and non-decomposing thermal protection systems. In AIAA, editor, *AIAA Aviation Forum*, 2015.
- [9] Frank P. Incropera, David P. DeWitt, Theodore L. Bergman, and Adrienne S. Lavine. *Fundamentals of Heat and Mass Transfer*. Wiley, Hoboken, NJ, 7th edition, 2011.
- [10] R. J. Klock and Carlos Cesnik. Nonlinear thermal reduced-order modeling for hypersonic vehicles. *AIAA Journal*, 55(7), 2017.
- [11] Arun Govind Neelan. Linear and non-linear reduced order model of scramjet. In *Advances in Multidisciplinary Design, Analysis and Optimization*, pages 111–118, Singapore, 2025.
- [12] Alberto Padovan, Blaine Vollmer, Francesco Panerai, Marco Panesi, Kelly A. Stephani, and Daniel J. Bodony. An extended bformulation for ablating-surface boundary conditions. *International Journal of Heat and Mass Transfer*, 218:124770, 2024.
- [13] Eric Parish and Karthik Duraisamy. Non-markovian closure models for large eddy simulations using the mori-zwanzig formalism. *Phys. Rev. Fluids*, 2:014604, Jan 2017.
- [14] Eric Parish and Karthik Duraisamy. A unified framework for multiscale modeling using the mori-zwanzig formalism and the variational multiscale method. *ArXiv*, 12 2017.
- [15] Eric Parish and Karthik Duraisamy. *Coarse-Graining Turbulence Using the Mori-Zwanzig Formalism*. Cambridge University Press, Cambridge, 2025.
- [16] Adam Thelen, Xiaoge Zhang, Olga Fink, Yan Lu, Sayan Ghosh, Byeng D. Youn, Michael D. Todd, Sankaran Mahadean, Chao Hu, and Zhen Hu. A comprehensive review of digital twin – part 1: modeling and twinning enabling technologies. *Structural and Multidisciplinary Optimization*, 65(12), 2022.

- 716 [17] Carlos A. Vargas Venegas, Daning Huang, Patrick Blonigan, and John Tencer. Physics-  
717 infused reduced-order modeling for analysis of multi-layered hypersonic thermal protec-  
718 tion systems, 2025.
- 719 [18] Yongyong Xian, Baisong Pan, and Luping Luo. A new model updating strategy with  
720 physics-based and data-driven models. *Structural and Multidisciplinary Optimization*,  
721 64(1), 2021.
- 722 [19] Yin Yu, John Harlim, Daning Huang, and Yan Li. Learning coarse-grained dynamics  
723 on graph. *arXiv preprint arXiv:2405.09324*, 2024.